

# A UNIFORMLY SELECTED SAMPLE OF LOW-MASS BLACK HOLES IN SEYFERT 1 GALAXIES. II. THE SDSS DR7 SAMPLE

He-Yang Liu<sup>1,2,4</sup>, Weimin Yuan<sup>1,2</sup>, Xiao-Bo Dong<sup>3</sup>, Hongyan Zhou<sup>4,5</sup> and Wen-Juan Liu<sup>3</sup>

## ABSTRACT

A new sample of 204 low-mass black holes (LMBHs) in active galactic nuclei (AGNs) is presented with black hole masses in the range of  $(1 - 20) \times 10^5 M_{\odot}$ . The AGNs are selected from a systematic search among galaxies in the seventh Data Release (DR 7) of the Sloan Digital Sky Survey (SDSS), by careful analyses of their optical spectra and precise measurement of spectral parameters. Combining them with our previous sample selected from the SDSS DR 4 makes it the largest LMBH sample so far, totaling over 500 objects. Some of the statistical properties of the combined LMBH AGN sample are briefly discussed, in the context of exploring the low-mass end of the AGN population. Their X-ray luminosities follow the extension of the previously known correlation with the [O III] luminosity. The effective optical-to-X-ray spectral indices  $\alpha_{\text{OX}}$ , albeit with a large scatter, are broadly consistent with the extension of the relation with the near-UV luminosity  $L_{2500\text{\AA}}$ . Interestingly, a correlation of  $\alpha_{\text{OX}}$  with black hole mass is also found in the sense that  $\alpha_{\text{OX}}$  is statistically flatter (stronger X-ray relative to optical) for lower black hole mass. Only 26 objects, mostly radio loud, were detected in radio at 20 cm in the FIRST survey, giving a radio loud fraction of 4%. The host galaxies of LMBHs have stellar masses in the range of  $10^{8.8} - 10^{12.4} M_{\odot}$  and optical colors typical of Sbc spirals. They are dominated by young stellar populations which seem to have undergone a continuous star formation history.

---

<sup>1</sup>Key Laboratory of Space Astronomy and Technology, National Astronomical Observatories, Chinese Academy of Sciences, 20A Datun Road, Chaoyang District, Beijing, 100012, China; wmy@nao.cas.cn, liuheyang@nao.cas.cn

<sup>2</sup>School of Astronomy and Space Sciences, University of Chinese Academy of Sciences, 19A Yuquan Road, Beijing, 100049, China

<sup>3</sup>Yunnan Observatories, Chinese Academy of Sciences, Kunming, Yunnan 650011, China; Key Laboratory for the Structure and Evolution of Celestial Objects, Chinese Academy of Sciences, Kunming, Yunnan, 650011, China; xbdong@ynao.ac.cn

<sup>4</sup>Polar Research Institute of China, 451 Jinqiao Road, Shanghai 200136, China

<sup>5</sup>The University of Sciences and Technology of China, Chinese Academy of Sciences, Hefei, Anhui, 230026, China

*Subject headings:* galaxies: active — galaxies: nuclei — galaxies: Seyfert

## 1. INTRODUCTION

Mounting evidence has been accumulated suggesting that many massive galaxies harbor supermassive black holes (SMBHs) with masses ranging from  $10^6 M_\odot$  to  $10^9 M_\odot$  at their centers in the present universe (e.g., [Richstone et al. 1998](#); [Kormendy & Ho 2013](#)). The mass of SMBHs correlates tightly with the parameters of the host bulges such as mass, luminosity and velocity dispersion, which hints at a picture of co-evolution of SMBHs and their host galaxies (e.g., [Magorrian et al. 1998](#); [Ferrarese & Merritt 2000](#); [Gebhardt et al. 2000a](#); [Gültekin et al. 2009](#)). How black holes (BHs) have formed across the cosmic time remains far from comprehension. It is commonly believed that SMBHs have grown from seed black holes through mainly merger-induced accretion ([Volonteri 2010](#); [Greene 2012](#)). Secular processes also play a role in BH growth, especially for BHs located in low-redshift galaxies ([Jiang et al. 2011](#); [Greene et al. 2008](#); [Conselice et al. 2014](#)). However, even less is known regarding the properties of seed BHs such as their origins, initial masses and environments, simply because direct observations of seed BHs in the early universe are not feasible with current facilities. As an indirect approach, low-mass black holes (LMBHs) with masses of thousands to hundreds of thousands of solar masses, residing at the center of galaxies, may help give insight into the formation and evolution of the first seed black holes. Such BHs are also termed intermediate-mass black holes (IMBHs) in the literature. We refer to them as LMBHs to avoid confusion from Ultra-luminous X-ray sources (ULXs), which are off-nucleus point-like sources and some may be powered by IMBHs ([Kaaret et al. 2017](#)). LMBHs found in nearby dwarf stellar systems in the present universe seem to have formed early, but have not fully grown into SMBHs ([Greene 2012](#)). They may thus trace the seed BHs or the early phase of their growing. In addition, the study of the occupation fraction of the present-day LMBHs can help discriminate various seed BH models, such as light seeds as the end-products of Population III stars or heavy seeds formed from the direct collapse of halos at high redshifts (e.g., [Volonteri et al. 2008](#); [Volonteri & Natarajan 2009](#); [Lodato & Natarajan 2006](#)). Interestingly, mergers of binary BHs with masses of the order of  $10^5 M_\odot$  can produce gravitational-wave signatures (e.g., [Hughes 2002](#)) that are the primary targets of LISA<sup>1</sup> in the future. The detection of gravitational waves in these frequency regimes has become more promising after the prototypical event GW150914, the first-ever gravitational-wave source detected by the Laser Interferometer Gravitational-wave Observatory (LIGO; e.g., [Abbott et al. 2016](#)).

---

<sup>1</sup>Laser Interferometer Space Antenna (LISA) is a space-based gravitational wave observatory led by the European Space Agency (ESA), designed to detect and accurately measure gravitational waves. The new LISA mission (based on the 2017 L3 competition) is a collaboration of ESA and NASA.

The most direct and secure way to detect BHs at the center of galaxies is to seek the effect of their gravitational influence on the spatially resolved dynamics of closely surrounding gases and/or stars (e.g., [Barth et al. 2001](#); [Ghez et al. 2008](#)). However, for LMBHs, this method is infeasible for distant galaxies since the BH gravitational sphere of influence can only be spatially resolved within the Local Group with the existing facilities. A common practice is to search for accretion-powered radiative signatures of active galactic nuclei (AGNs) hosting such LMBHs. For AGNs exhibiting broad emission lines in their optical spectra, their BH masses can be estimated using  $M_{\text{BH}} = fRv^2/G$ , assuming that the broad line region (BLR) system is virialized and individual clouds are moving in Keplerian orbits.  $G$  is the gravitational constant. The velocity dispersion  $v$  can be measured from the widths of the broad emission lines. The BLR radius  $R$  is estimated from the luminosity of AGN continuum emission using the radius-luminosity relation derived from reverberation mapping studies of AGNs (e.g., [Kaspi et al. 2005](#); [Bentz et al. 2006, 2009, 2013](#)).  $f$  is a scaling factor of the order of unity, depending on the distribution and inclination of the BLR-cloud orbits to the line of sight, and can be calibrated from other independent measurements of the same BH systems. BH masses thus estimated are indirect and subject to systematics as large as  $\sim 0.3$  dex (e.g., [Gebhardt et al. 2000b](#); [Greene & Ho 2006](#); [Grier et al. 2013](#)). Nevertheless, they provide us one of the fundamental parameters to study the vast majority of the AGN population. An archetypal LMBH AGN is NGC 4395 ([Filippenko & Ho 2003](#)), which is a bulgeless galaxy harboring a central BH of  $M_{\text{BH}} \sim 3 \times 10^5 M_{\odot}$  measured through reverberation mapping observations of the C IV  $\lambda 1549$  line ([Peterson et al. 2005](#)). Multi-wavelength observations in the X-ray (e.g., [Iwasawa et al. 2000](#); [Moran et al. 2005](#); [Dewangan et al. 2008](#)) and Radio bands (e.g., [Wrobel & Ho 2006](#)) support the finding of a small BH mass in NGC 4395. Other convincing cases of LMBH in AGNs include POX 52, a dwarf spheroidal galaxy with a BH of  $M_{\text{BH}} \sim 3 \times 10^5 M_{\odot}$  (e.g., [Barth et al. 2004](#); [Thornton et al. 2008](#)), and SDSS J160531.84+174826.1, a dwarf disk galaxy with a BH of  $M_{\text{BH}} \sim 7 \times 10^4 M_{\odot}$  ([Dong et al. 2007](#)).

In general, single-epoch optical spectrum is an effective tool of detecting signature of nuclear BHs in active galaxies. AGNs with LMBHs as large sample were first searched by [Greene & Ho \(2004, 2007a\)](#) from the Sloan Digital Sky Survey (SDSS; [York et al. 2000](#)) yielding  $\sim 200$  broad-line sources with the BH masses in the range of  $\sim 10^{5-6} M_{\odot}$ , estimated from the widths and luminosities of the broad H $\alpha$  emission lines. Independently we ([Dong et al. 2012](#), hereafter Dong+12) carried out a systematic and homogeneous search for LMBHs from the SDSS Fourth Data Release (DR4; [Adelman-McCarthy et al. 2006](#)), resulting in 309 AGNs, with relatively lower BH mass and Eddington ratio distributions. In recent surveys targeting low-mass type 2 AGNs, there are more than one hundred sources in nearby dwarf galaxies identified as LMBH candidates using narrow-line diagnostics (e.g., [Barth et al. 2008](#); [Reines et al. 2013](#); [Moran et al. 2014](#)). According to [Yuan et al. \(2014\)](#), if the intrinsic Eddington ratio distribution of SMBHs obtained by [Schulze & Wisotzki \(2010\)](#) can be applied to the low-mass end, there should exist many more

LMBHs in the universe. Clearly, a larger LMBH sample than the current ones homogeneously selected with well-understood completeness is essential to construct the intrinsic Eddington ratio and mass functions (Liu et al. 2018 in prep.). These will give more stringent constraints on seed black hole models. Moreover, a statistical study of the interplay of LMBH AGNs and their host galaxies also requires a larger sample, especially at the lower- $M_{\text{BH}}$  and lower-accretion-rate end. In this work, we perform an extended search for more low-mass AGNs from the SDSS Seventh Data Release (DR7; Abazajian et al. 2009), on the basis of our previous work using the SDSS DR4 (Dong+12).

It is difficult to search for AGNs with low-mass black holes since their optical spectra are mostly strongly dominated by starlight. Thus careful subtraction of the starlight is essential for reliable measurement of the emission lines. In addition, the decomposition of the broad and the narrow components of the Balmer lines in LMBH AGNs is delicate as the broad lines in the spectra of LMBHs are relatively narrow and weak<sup>2</sup>. In order to search for LMBHs, we have designed a set of elaborate codes and broad-line selection procedures as described in Dong+12. In this work, we follow exactly the same method and apply it to the SDSS DR7. Some 204 new LMBHs are found with  $M_{\text{BH}} < 2 \times 10^6 M_{\odot}$  (to be in accordance with the Greene & Ho 2007a and Dong+12), expanding the total SDSS sample of LMBHs to 513. The BH masses of the new sample range from  $1 \times 10^5 M_{\odot}$  to  $2 \times 10^6 M_{\odot}$ , with a median of  $1.3 \times 10^6 M_{\odot}$ , and the Eddington ratios range from  $\sim 0.01$  to  $\sim 1$ . The data analysis and sample selection are outlined in Section 2, respectively, and the LMBH sample is described in Section 3. In Section 4, the sample properties are discussed, followed by a summary in Section 5. Throughout the paper we assume a cosmology with  $H_0 = 70 \text{ km s}^{-1} \text{ Mpc}^{-1}$ ,  $\Omega_m = 0.3$ , and  $\Omega_{\Lambda} = 0.7$ .

## 2. DATA ANALYSIS AND SAMPLE SELECTION

Our LMBH AGNs are selected following the data analysis procedures described in Dong+12, which are only briefly summarized here (see Dong+12 for details). We start from the SDSS DR7 spectra classified as “galaxies” or “QSOs” by the SDSS pipeline, excluding objects also in the SDSS DR4. The SDSS is a comprehensive imaging and spectroscopic survey using a dedicated 2.5 m telescope (Gunn et al. 2006) located at the Apache Point Observatory in Southern New Mexico. It utilizes a wide-field imager (Gunn et al. 1998) covering the sky in a drift-scan mode in five

---

<sup>2</sup> According to Dong+12, the broad  $H\alpha$  widths (FWHMs) of LMBHs range from 500 to 2200  $\text{km s}^{-1}$ , with a median of 1000  $\text{km s}^{-1}$ , which is much lower than that of the entire parent broad-line AGN sample ( $\approx 3000 \text{ km s}^{-1}$ ) and even slightly smaller than the traditional demarcation value between AGN broad and narrow lines (1200  $\text{km s}^{-1}$ ; cf. Hao et al. 2005).

filters *ugriz* (Fukugita et al. 1996), and a 640-fiber-fed pair of multi-objects double spectrographs covering the wavelength 3800–9200 Å with a resolution of  $\lambda/\Delta\lambda \approx 2000$ . The diameter of the optical fibers is 3'' and the instrumental dispersion is  $\sim 69 \text{ km s}^{-1} \text{ pixel}^{-1}$ . To ensure the  $\text{H}\alpha$  lying within the wavelength coverage range of the SDSS spectra, only sources with redshifts below 0.35 are considered. These result in a parent sample consisting of 337,988 “galaxies” and 4,697 “QSOs”. The spectra are corrected for the Galactic extinction using the extinction map of Schlegel et al. (1998) and the reddening curve of Fitzpatrick (1999), and are then transformed to the rest frame with the redshifts provided by the SDSS pipeline.

The spectra of the parent sample are mostly dominated by starlight. As the first step, a pseudo-continuum is modeled and subtracted using the technique described in Zhou et al. (2006)<sup>3</sup>. The so-called pseudo-continuum is a linear combination of several components, including starlight, nuclear continuum and the optical Fe II multiplets. The Balmer continua and high order Balmer emission lines are added if it can improve the reduced  $\chi^2$  by at least 20%. The stellar component is modeled by six synthesized galaxy spectral templates built up from the library of simple stellar populations (SSPs; Bruzual & Charlot 2003) using the Ensemble Learning Independent Component Analysis algorithm (Lu et al. 2006), which takes all the stellar features into account and can thus significantly mitigate the problem of overfitting. A power law is adopted to describe the AGN continuum. The optical Fe II multiplets are modeled by two separate sets of templates constructed by Dong et al. (2008, 2011) based on the measurements of IZw 1 by Véron-Cetty et al. (2004), one for broad lines and the other for narrow lines.

The next step is to fit the emission lines and to select broad-line candidates. We focus on the broad  $\text{H}\alpha$  line ( $\text{H}\alpha^{\text{B}}$ ) since it is the strongest broad line in the optical spectra of AGNs. Our initial criteria for the addition of a broad component of  $\text{H}\alpha$  are as follows<sup>4</sup>. (1) It would result in a significant decrease in  $\chi^2$  with a chance probability of F-test  $< 0.05$ , (2) the width of  $\text{H}\alpha^{\text{B}}$  is relatively larger than those of narrow lines, particularly [O III]  $\lambda 5007$ , (3)  $\text{H}\alpha^{\text{B}}$  has a statistically significant flux, namely,  $\text{Flux}(\text{H}\alpha^{\text{B}}) > 3\sigma$ ,  $\sigma$  is the statistical noise, (4)  $\text{Flux}(\text{H}\alpha^{\text{B}}) > 10^{-16} \text{ erg s}^{-1} \text{ cm}^{-2}$ . After removing the continua, the residual spectra are first fitted in order to remove objects without any broad lines according to our selection criteria, resulting in a significant reduction of the number of objects needing refined fitting ( $\sim 303,000$  objects are removed). Next, the  $\text{H}\alpha$  region is initially modeled using pure narrow line profiles without broad component. The narrow  $\text{H}\alpha$  + [N II]  $\lambda\lambda 6548, 6583$  lines are fitted with a narrow-line model built up from the [S II]  $\lambda\lambda 6716, 6731$

---

<sup>3</sup>Note that there exists a population of spectra dominated by AGNs, of which the starlight components are negligible and the broad lines are broad and significant. For the case we fit simultaneously the AGN power-law continuum together with the emission lines including the Fe II multiplets, the forbidden and the Balmer lines (details see Dong et al. 2008).

<sup>4</sup>Details see Section 3 of Dong+12.

doublets, or from the core of [O III]  $\lambda\lambda 4959, 5007$  if [S II] is weak. The profiles and redshifts of H $\alpha$  and the [N II] doublets are assumed to be the same as the narrow-line model obtained above. The centroid wavelengths of these narrow lines, as well as the flux ratios of the [N II] doublets  $\lambda 6583/\lambda 6548$  and the [O III] doublets  $\lambda 5007/\lambda 4959$  are fixed to their theoretical values, respectively. Then, a possible additional broad component of H $\alpha$  is considered if it satisfies the broad line criteria. This step results in  $\sim 17500$  spectra leftover in which a candidate broad H $\alpha$  component may be present.

The broad H $\alpha$  lines of LMBH AGNs are generally relatively narrow and/or weak, and their fluxes are susceptible to the subtraction of the narrow lines. Thus for the remaining  $\sim 17500$  spectra, we employ a series of schemes to fit the narrow H $\alpha$  line, including narrow-line profiles built up from narrow H $\beta$ , [S II], [O III] or [N II], respectively. The result with the minimum reduced  $\chi^2$  is adopted as the best fit. An example spectrum and the best fitted model are shown in Figure 1.

To ensure the reliability of the existence of a broad component, we apply further a more strict cut on the signal-to-noise ratio of the broad H $\alpha$  flux,  $S/N(H\alpha^B) \geq 5$ , where  $S/N(H\alpha^B)$  is the ratio of the broad H $\alpha$  flux to the total uncertainties ( $\sigma_{\text{total}}$ ),  $S/N(H\alpha^B) = \text{Flux}(H\alpha^B) / \sigma_{\text{total}}$ .  $\sigma_{\text{total}}$  is the quadrature sum of statistical noise ( $\sigma_{\text{stat}}$ ), the uncertainties arising from subtraction of the continuum ( $\sigma_{\text{cont\_sub}}$ ) and the noise caused by the subtraction of the narrow lines ( $\sigma_{\text{NL\_sub}}$ ), namely,  $\sigma_{\text{total}}^2 = \sigma_{\text{stat}}^2 + \sigma_{\text{NL\_sub}}^2 + \sigma_{\text{cont\_sub}}^2$ . The  $\sigma_{\text{NL\_sub}}$  is estimated using the rest  $n$  sets of fitting results that are worse than the best one and with the chance-probability of the F-test greater than 0.1,

$$\sigma_{\text{NL\_sub}} = \sqrt{\frac{\sum_{i=1}^n (\text{Flux}(H\alpha^B)_i - \text{Flux}(H\alpha^B)_{\text{best}})^2}{n}}. \quad (1)$$

As for  $\sigma_{\text{cont\_sub}}$ , the term is negligible since the H $\alpha$  absorption features are weak in most cases and the continuum decomposition for each broad-line AGN candidate has been visually checked to ensure that the subtraction error is much below  $1 \sigma$ . With the cut of  $S/N(H\alpha^B)$ , we obtain 6092 objects with reliable broad H $\alpha$  detections, including 1,850 “galaxies” and 4,242 “QSOs”.

### 3. LMBH AGN SAMPLE FROM THE SDSS DR7

The optical spectra of low-mass AGNs are often substantially contaminated by starlight and it is difficult to directly measure the continuum luminosities. Thus the luminosities of the broad Balmer lines are adopted to estimate the BH masses. In this study, for ease of comparison, the BH masses are calculated using the formalism presented in GH07 following Dong+12,

$$M_{\text{BH}} = (3.0^{+0.6}_{-0.5}) \times 10^6 \left( \frac{L_{\text{H}\alpha^B}}{10^{42} \text{ erg s}^{-1}} \right)^{0.45 \pm 0.03} \left( \frac{\text{FWHM}_{\text{H}\alpha^B}}{10^3 \text{ km s}^{-1}} \right)^{2.06 \pm 0.06} M_{\odot}. \quad (2)$$

The formalism was derived using the empirical correlations of  $\lambda L_\lambda(5100 \text{ \AA})-L_{\text{H}\alpha^{\text{B}}}$  and  $\text{FWHM}_{\text{H}\alpha^{\text{B}}}-\text{FWHM}_{\text{H}\beta^{\text{B}}}$  from [Greene & Ho \(2005\)](#)<sup>5</sup>, along with the radius-luminosity relation reported by [Bentz et al. \(2006\)](#). Finally a sample of 204 objects with BH masses less than  $2 \times 10^6 M_\odot$ <sup>6</sup> are obtained. Table 1 summarizes the basic data of the sample. The emission line parameters obtained from the best-fit models as described in Section 2.1, are tabulated in Table 2 and Table 3, along with the BH mass and luminosity. The flux of Fe II  $\lambda 4570$  is calculated by integrating the flux density of the corresponding Fe II multiplets from 4434 Å to 4684 Å in the rest-frame.

Our sample has a median redshift of 0.1 (see Figure 2) and BH masses ranging from  $1.1 \times 10^5 M_\odot$  to  $2.0 \times 10^6 M_\odot$ . The FWHMs of  $\text{H}\alpha^{\text{B}}$  span a range of  $\sim 500-2200 \text{ km s}^{-1}$ , with a median of  $1000 \text{ km s}^{-1}$ . The broad Ha line luminosities  $L_{\text{H}\alpha^{\text{B}}}$  are in the range of  $\sim 10^{39.3}-10^{42.1} \text{ erg s}^{-1}$  with a median lying at  $10^{39.3} \text{ erg s}^{-1}$ . We caution that dust extinction may attenuate the observed broad  $\text{H}\alpha$  flux for some of the low-mass AGN and may lower somewhat the measured  $L_{\text{H}\alpha^{\text{B}}}$ . Given that the measurement of the broad  $\text{H}\beta$  line in low-mass AGN suffer large uncertainties, it is difficult to quantify the dust reddening effect. Following GH07 and Dong+12, we do not correct for the dust reddening in this work. The Eddington ratio ( $L_{\text{bol}}/L_{\text{Edd}}$ ) is defined as the ratio of the bolometric luminosity ( $L_{\text{bol}}$ ) to the Eddington luminosity ( $L_{\text{Edd}} = 1.26 \times 10^{38} M_{\text{BH}}/M_\odot$ ).  $L_{\text{bol}}$  is derived from the optical luminosities at 5100 Å using a bolometric correction factor of 9.8 ([McLure & Dunlop 2004](#)),  $L_{\text{bol}} = 9.8 \lambda L_\lambda(5100 \text{ \AA})$ , where  $\lambda L_\lambda(5100 \text{ \AA})$  is derived from the broad  $\text{H}\alpha$  luminosity using the scaling relation given in [Greene & Ho \(2005\)](#). The Eddington ratios thus estimated for the current LMBH sample range from 0.01 to 2. Figure 3 and Figure 4 show the distributions of BH masses and Eddington ratios, as well as the luminosities and FWHMs of broad  $\text{H}\alpha$ , for our sample. Those of the Dong+12 and GH07 samples are also plotted for comparison.

As expected, the distributions of the DR7 LMBHs are similar to those in Dong+12. The median  $M_{\text{BH}}$  of the present sample is  $1.3 \times 10^6 M_\odot$ , comparable to  $1.2 \times 10^6 M_\odot$  of Dong+12. As for  $L_{\text{bol}}/L_{\text{Edd}}$ , the medians are  $-0.59$  and  $-0.64$  in log-scale, respectively. The medians of  $L_{\text{H}\alpha^{\text{B}}}$  and  $\text{FWHM}_{\text{H}\alpha^{\text{B}}}$  for the current sample and Dong+12 are very close ( $41.00$  versus  $40.99$  and  $2.99$  versus  $3.02$ , calculated in logarithm, respectively). In addition, the standard deviations of these quantities, including  $M_{\text{BH}}$ ,  $L_{\text{bol}}/L_{\text{Edd}}$ ,  $L_{\text{H}\alpha^{\text{B}}}$  and  $\text{FWHM}_{\text{H}\alpha^{\text{B}}}$ , of the two samples are consistent within 0.07 dex.

---

<sup>5</sup>In fact, [Greene & Ho \(2005\)](#) gives the correlation between  $\lambda L_\lambda(5100 \text{ \AA})$  and the combined  $\text{H}\alpha$  luminosity of both broad and narrow components. However, as described in [Greene & Ho \(2005\)](#), “the best-fit parameters are virtually unchanged when only the broad component is considered”. In addition, the narrow  $\text{H}\alpha$  component may be contaminated by the host galaxies for our LMBHs. Thus in this study  $\lambda L_\lambda(5100 \text{ \AA})$  is estimated using merely broad  $\text{H}\alpha$  component.

<sup>6</sup>We adopt the same upper limit of LMBHs as in GH07 and Dong+12 for consistency.

## 4. SAMPLE PROPERTIES

In combination with the 309 objects in Dong+12, we expand the SDSS LMBH AGN sample to a total of 513 sources up to the DR7. This is the largest sample of low-mass AGNs so far, which have the uniform and homogeneous selection criteria and well measured AGN parameters, thanks to the homogeneity and accurate spectrophotometry of the SDSS. It is worthwhile to investigate the statistical properties for the total sample. In this section we present some of the ensemble properties of the LMBH AGNs and their host galaxies based on the SDSS data, as well as data from X-ray and Radio surveys.

### 4.1. Narrow Line Diagnostic Diagrams

Compared with H II galaxies, AGN can emit a harder continuum which results in a distinct ionization condition in surrounding gas. Specific emission line ratios can help distinguish the central radiating sources that ionize the circumnuclear medium. In practice, two-dimensional diagrams of certain narrow-line ratios have been widely applied to discriminate between H II galaxies and type 2 AGNs (e.g., Baldwin et al. 1981; Veilleux & Osterbrock 1987; Ho et al. 1997a; Kewley et al. 2001, 2006; Kauffmann et al. 2003b). The so-called BPT diagrams involving the narrow line ratios of  $H\alpha$ ,  $H\beta$ , [O III], [N II], [S II], and [O I] are shown in Figure 5. In general, the distributions of our LMBHs are consistent with those of Dong+12. On the [O III]  $\lambda 5007/H\beta$  versus [N II]  $\lambda 6583/H\alpha$  diagram (panel (a)), the vast majority of these LMBHs are located in the region of either Seyfert galaxies or composite objects, and only a few sources ( $\sim 10$ ) fall into the pure star-forming region. On the diagrams of the [O III]  $\lambda 5007/H\beta$  versus [S II]  $\lambda\lambda 6716, 6731/H\alpha$  and [O I]  $\lambda 6300/H\alpha$  diagrams (panels (b) and (c)), about two-thirds of these objects are found in the AGN region, while the rest are located in the H II region.

These results confirm the AGN nature for the vast majority of our sample, though a few objects have the narrow-line spectra similar to those of star-forming galaxies. Regarding those objects located in the pure H II portion, their broad  $H\alpha$  fluxes, FWHMs and luminosities are all similar to those of the whole parent sample, with chance probabilities  $> 0.1$  according to Kolmogorov–Smirnov test (KS test). Visual checks of their SDSS spectra and the statistics (broad  $H\alpha$  flux with  $S/N > 5$ ) both demonstrate that the broad  $H\alpha$  components of these objects are significant and reliable. A probable explanation is that the spectra of these objects are strongly contaminated by star light from those star-formation regions in the host galaxies, given the relatively large aperture of the fiber of  $3''$ .

We note that about two dozens of objects fall into the region of low-ionization nuclear emission-line region sources (LINERs; Heckman 1980) according to the Seyfert–LINER demarcation lines

of either  $[\text{O III}] \lambda 5007/\text{H}\beta = 3$  in panel (a) or Kewley et al. (2006) in panels (b) and (c). LINERs are commonly found in early-type galaxies with classical bulges containing supermassive BHs especially with old stellar populations (Ho et al. 1997b). LMBHs tend to reside in late type disk-dominated galaxies often harboring pseudobulges just on the opposite. Therefore such LMBH LINERs are of great interest to study LINERs as a population though it is not a surprise that only a small number of low-mass AGNs show LINER-like spectra. Mostly manifesting themselves as low-luminosity AGNs, LINERs are thought to have relatively low accretion rates and their accretion flows are dominated by ADAF (Advection-Dominated Accretion Flow; see e.g., Kewley et al. 2006; Ho 2009; Narayan & Yi 1995). The combination of low BH mass and low accretion rate make it even difficult to identify LINERs with LMBHs in the presence of host galaxy light. These may explain the low incidence of LINERs in the LMBH sample.

## 4.2. X-ray Properties

X-ray is an important bandpass to study BH accretion. A number of LMBH AGNs in the GH07 sample have been observed in X-ray with *Chandra* (e.g., Greene & Ho 2007b; Desroches et al. 2009; Dong R. et al. 2012), which gave a snapshot for the X-ray properties of LMBHs. Focusing on low-mass AGNs with very low Eddington ratios ( $L_{\text{bol}}/L_{\text{Edd}} \sim 0.01$ ), i.e., the faintest AGN population known, Yuan et al. (2014) studied the X-ray properties of four objects observed by *Chandra* in the Dong+12 sample, and suggested there should exist a large population of underluminous LMBHs in the nearby universe. Plotkin et al. (2016) performed a similar analysis on seven low-mass black holes with low Eddington ratios from GH07 using *Chandra* observations. The two well-studied LMBHs, NGC 4395 and POX 52, were found to show rapid and strong X-ray variabilities (e.g., Iwasawa et al. 2000; Moran et al. 2005; Dewangan et al. 2008; Thornton et al. 2008). Their spectral characteristics resemble those classical Seyfert 1 galaxies. Miniutti et al. (2009) performed a detailed analysis on four LMBHs from Greene & Ho (2004) using *XMM-Newton* observations, finding that they are extremely variable and three out of the four objects show soft excess in their spectra. Similarly, Ludlam et al. (2015) followed a study with 14 LMBHs from GH07 with *XMM-Newton*, eight of which show soft excess emissions. In addition, LMBHs also present diverse timing properties. In general, LMBHs tend to show larger X-ray variability amplitude than their more massive cousins. Pan et al. (2015) and Ludlam et al. (2015) showed the previous known inverse correlation between  $M_{\text{BH}}$  and the normalized excess variance of X-ray variability, and flattens at  $M_{\text{BH}} \sim 10^6 M_{\odot}$  and thus vanishes for LMBH AGNs.

In this study, we briefly investigate the statistical X-ray properties of the total sample of 513 sources based on the *ROSAT* All-Sky Survey (RASS, Boller et al. 2016) and pointed observations (2RXP). Detailed X-ray spectral and timing analysis using *XMM-Newton* are deferred to later

work.

#### 4.2.1. X-ray Detection

Of the 513 sources, 85 were detected by the RASS and 32 in pointed observations, with 15 detected in both (for these sources, the data from the pointed observations are adopted). Thus a total of 102 objects have X-ray detections with the *ROSAT* Positional Sensitive Proportional Counter (PSPC). Their X-ray fluxes and spectral indices in the 0.1–2.4 keV band are estimated following Schartel et al. (1996) and Yuan et al. (1998, 2008), assuming an absorbed power-law spectral shape. As the first step, the photon index  $\Gamma$  is calculated from the two hardness ratios<sup>7</sup> if available. The absorption column density  $N_{\text{H}}$  is fixed at the Galactic value (Dickey & Lockman 1990), or set to a free parameter if no meaningful  $\Gamma$  is obtained using the Galactic  $N_{\text{H}}$ . For those sources without meaningful hardness ratios, the mean value ( $\Gamma = 2.36$ ) is adopted. Next we estimate the X-ray fluxes in the 0.1–2.4 keV band from the count rates using the energy-to-counts conversion factor (ECF; *ROSAT* AO-2 technical appendix, 1991), which is calculated from the *ROSAT* PSPC effective area for each source, for the given power-law spectrum with  $\Gamma$  and  $N_{\text{H}}$  obtained above. The X-ray fluxes in the band of 0.5–2.0 keV are tabulated in Table 4, which range from  $1.8 \times 10^{-14}$  to  $2.9 \times 10^{-12}$  erg s<sup>-1</sup> cm<sup>-2</sup>. The corresponding luminosities span a range from  $8.0 \times 10^{39}$  to  $1.1 \times 10^{44}$  erg s<sup>-1</sup>, comparable to  $9.3 \times 10^{39}$ – $6.9 \times 10^{43}$  erg s<sup>-1</sup> for GH07 sample. This indicates that the X-ray emission is mostly dominated by AGN radiation, since the X-ray luminosities of normal galaxies are generally below this level.

For those undetected by the *ROSAT*, upper limits on the X-ray fluxes are estimated using the method in Yuan et al. (2008). An upper limit of 12 source counts is adopted for each undetected object, and thus the count rate upper limit is calculated using the corresponding effective exposure time from the RASS exposure map. Then the flux upper limits are estimated using the method described above assuming the Galactic  $N_{\text{H}}$  and the mean  $\Gamma$  of 2.36.

#### 4.2.2. X-ray versus [O III] $\lambda$ 5007 Luminosity

The soft X-ray emission is susceptible to absorption, while the [O III] luminosity is suggested to be an isotropic indicator of the intrinsic AGN power since the [O III] line originates from the narrow-line region and should be unaffected by obscuration. A strong correlation between the X-

---

<sup>7</sup>The two hardness ratios are defined as  $\text{HR1} = (B - A)/(B + A)$ ,  $\text{HR2} = (D - C)/(D + C)$ , where A, B, C and D are the number of source counts in the energy channels of 11–41, 52–201, 52–90 and 100–201 respectively.

ray and [O III]  $\lambda 5007$  luminosity has been found in unobscured AGNs (e.g. Panessa et al. 2006). This can help to discriminate whether our low-mass AGNs are heavily obscured.

The relation between the 2–10 keV luminosity and [O III]  $\lambda 5007$  luminosity for the X-ray detected sources is shown in Figure 6, overplotted are the low-mass AGN sample with *ROSAT* detections from GH07, LMBHs observed by *Chandra* from Dong R. et al. (2012), more massive AGNs in Jin et al. (2012) and low-mass AGNs with  $\log(L_{\text{bol}}/L_{\text{Edd}}) < -1.5$  observed using *Chandra* in Yuan et al. (2014) and Plotkin et al. (2016). Luminosities in the 2–10 keV band are calculated by extrapolating the spectra of the *ROSAT* to 10 keV assuming a photon index of 2.5. The *ROSAT*-detected sources in our total sample are roughly consistent with the correlation between X-ray and [O III]  $\lambda 5007$  luminosity derived by more massive AGNs (Panessa et al. 2006). It indicates that our low-mass AGNs with X-ray detections suffer little or no obscuration in X-rays.

#### 4.2.3. Optical–X-ray Spectral Index

The optical/X-ray effective spectral index,  $\alpha_{\text{OX}} \equiv -0.384 \log(f_{2500\text{\AA}}/f_{2\text{keV}})$ , where  $f_{2500\text{\AA}}$  and  $f_{2\text{keV}}$  are the rest-frame flux densities at 2500  $\text{\AA}$  and 2 keV respectively, is commonly used to describe the relative dominance of the optical and X-ray emission (Tananbaum et al. 1979)<sup>8</sup>. The statistical properties of  $\alpha_{\text{OX}}$  have been well studied for the classical AGNs (e.g. Avni & Tananbaum 1986; Yuan et al. 1998; Vignali et al. 2003; Steffen et al. 2006). Recently, Dong R. et al. (2012) studied the  $\alpha_{\text{OX}}$  properties of 49 low-mass AGNs in the GH07 sample with *Chandra* observations. In this work, we briefly investigate the  $\alpha_{\text{OX}}$  properties of LMBHs based on *ROSAT* observations.

The  $\alpha_{\text{OX}}$  indices are calculated as follows.  $f_{2\text{keV}}$  is derived from the *ROSAT* observations as described in Section 4.2.1 and  $f_{2500\text{\AA}}$  is calculated from  $L_{\text{H}\alpha\text{B}}$  using the relation between  $L_{\text{H}\alpha\text{B}}$  and  $\lambda L_{\lambda}(5100\text{\AA})$  given by Greene & Ho (2005) assuming a spectral index of 1.56 ( $f_{\lambda} \propto \lambda^{-1.56}$ ; Vanden Berk et al. 2001). The  $\alpha_{\text{OX}}$  values are listed in Table 4, and their distribution is shown in Figure 7. The  $\alpha_{\text{OX}}$  distribution has a large scatter, ranging from  $-1.58$  to  $-0.70$ , with a median of  $\langle \alpha_{\text{OX}} \rangle = -1.12$ , which is systematically flatter than those of AGNs with more massive black holes (e.g.,  $\alpha_{\text{OX}} \sim -1.5$ ; Yuan et al. 1998). The  $\alpha_{\text{OX}}$  distribution of our low-mass is similar with that of the *ROSAT*-detected sources in GH07, but slightly flatter than that of the LMBHs with *Chandra* observations in Dong R. et al. (2012). These LMBHs are roughly in accordance with the relation between  $\alpha_{\text{OX}}$  and the monochromatic luminosity at 2500  $\text{\AA}$  defined by those more massive AGNs (Steffen et al. 2006), albeit with large scatter (see Figure 8). In addition, Figure 8 shows that low-mass AGNs have systematically flatter  $\alpha_{\text{OX}}$  and a larger scatter compared to those of more massive

---

<sup>8</sup>The definition is different from the original one in Tananbaum et al. (1979) by a negative sign.

black holes, which is consistent with that in [Dong R. et al. \(2012\)](#).

As can be seen from Figure 8, though the distribution of our LMBH AGNs are mostly confined within the  $1\sigma$  scatter of the  $\alpha_{\text{OX}}-L_{2500\text{\AA}}$  relationship, there is a much larger scatter when the *Chandra* samples of [Dong R. et al. \(2012\)](#) and [Yuan et al. \(2014\)](#) are taken into account, which contains some X-ray weak objects detected by *Chandra* owing to its high sensitivity. To explore further the large scatter of  $\alpha_{\text{OX}}$  for LMBH AGNs, we plot in Figure 9  $\alpha_{\text{OX}}$  versus the Eddington ratio and BH mass for our sample as well as the other AGN samples as in Figure 8. No significant correlation is found between  $\alpha_{\text{OX}}$  and  $L_{\text{bol}}/L_{\text{Edd}}$  over a wide range for the LMBHs spanning nearly two orders of magnitudes. This is consistent with previous results for LMBH AGNs (e.g., [Greene & Ho 2007b](#); [Dong R. et al. 2012](#)). Regarding the  $\alpha_{\text{OX}}-M_{\text{BH}}$  relationship, no correlation is found for LMBHs only given the narrow dynamic range of  $M_{\text{BH}}$ ; however, a weak correlation (Spearman’s rank correlation coefficient is  $-0.25$  with a null probability of  $\sim 10^{-7}$ ) appears to be present when taking into account AGNs with more massive BHs from the other samples, albeit the large dispersion for the LMBHs. A similar weak correlation was also suggested by [Dong R. et al. \(2012\)](#). Thus the wide  $\alpha_{\text{OX}}$  distribution for LMBH AGNs is not caused by the distributions of the Eddington ratio or BH mass.

Three possibilities might account for the large scatter in the  $\alpha_{\text{OX}}$  distribution. The first is X-ray variability. It has been demonstrated that the amplitude of short time-scale X-ray variability is anti-correlated with the BH mass for AGNs with  $M_{\text{BH}} > 10^6 M_{\odot}$  (e.g., [Ponti et al. 2012](#); [Kelly et al. 2013](#)), below which the relation flattens ([Pan et al. 2015](#); [Ludlam et al. 2015](#)). This means that LMBH AGNs show the largest amplitude of X-ray variability among all AGNs. Moreover, LMBH AGNs appear to show strong variations in the X-ray spectral shape, as manifested by their wide range of the spectral indices ( $\Gamma = 1.2-4.0$ ). A typical example is NGC 4395, which was found to exhibit rapid and strong X-ray variability ([Iwasawa et al. 2000](#); [Dewangan et al. 2008](#)), and its X-ray spectral slope varied from  $\Gamma < 1.25$  to  $\Gamma > 1.7$  in about one year ([Moran et al. 2005](#)). Similar behavior was also found in POX 52 ([Thornton et al. 2008](#)).

Secondly, LMBHs may have a wide distribution in the intrinsic X-ray luminosities. As commonly believed, the X-ray emission is mainly produced in the hot corona by inverse-Compton scattering of optical/UV photons from the disk. The relative dominance of the optical/UV and X-ray emission is determined by the fraction of the energy deposited into the hot corona out of the total viscos energy produced in the accretion disk. For instance, in models that the corona is heated by magnetic re-connection ([Liu et al. 2003](#)), the fraction is mainly determined by the magnetic field strength in the corona, which may vary from one object to another.

Thirdly, X-ray absorption may play a role as well. Although no strong effect of X-ray obscuration is present for most of the objects as suggested by the  $L_{2-10\text{keV}}-L_{[\text{OIII}]}$  relation above, moderate absorption cannot be ruled out in some of the objects. It is probable that the environment

of LMBH may be more gas-rich compared to normal AGNs powered by more massive BHs, whose stronger radiation makes it easier to expel circumnuclear materials.

### 4.3. Radio Properties

We explore the radio properties for our total LMBH sample using radio data at 20 cm from the VLA FIRST survey<sup>9</sup> (Becker et al. 1995). There are 26 objects detected, leading to a low detection fraction of 5%. The low incidence of radio activity is consistent with the result in GH07. The radio powers at 20 cm of these sources range from  $2 \times 10^{21}$  to  $4 \times 10^{23}$  W Hz<sup>-1</sup>, with a median of  $4 \times 10^{22}$  W Hz<sup>-1</sup> (see Table 5). Figure 10 shows their radio power versus the [O III] luminosity, which appears broadly consistent with what is found in GH07.

As a common practice, the radio loudness parameter, defined as the radio to optical flux ratio ( $R \equiv f_{6\text{cm}}/f_{4400\text{\AA}}$ ), is used to separate radio-loud AGNs from radio-quiet ones, with an operational dividing value of 10. The radio loudness is calculated for the radio-detected sources as following:  $f_{6\text{cm}}$  is derived assuming a radio spectral index of  $\alpha_r = 0.46$  ( $f_\nu \propto \nu^{-\alpha_r}$ ; Ulvestad & Ho 2001) from the flux density at 20 cm; while  $f_{4400\text{\AA}}$  is estimated in the same way as  $f_{2500\text{\AA}}$ . Among the 26 sources with FIRST detections, 23 are radio loud, corresponding to a radio loud fraction of 4%. For those sources undetected in FIRST<sup>10</sup>, upper limits on radio loudness are estimated assuming a radio flux density of 1 mJy at 20 cm, which is the detection limit of the FIRST survey (see Figure 11).

The radio loud fraction in the LMBH AGN sample is lower than that of classical AGNs ( $\sim 15\%$ ; Ivezić et al. 2002). This seems to be consistent with the finding that radio sources may prefer to reside in more massive galaxies (Best et al. 2005). For our LMBHs, their host galaxies are indeed at the lower-stellar-mass end of the parent sample from the SDSS DR7 (see Section 5.3 for details). However, it should be noted that, the above radio loud fraction should only be considered as a lower limit, since the FIRST flux sensitivity is not deep enough to give stringent constraints on the radio loudness. Further deep and high spatial resolution radio surveys are needed to determine the true radio loud fraction for LMBHs.

As a natural interpretation, the radio emission of an active galaxy is a mixture of contribution from nuclear AGNs and star formation in the host galaxy. This may be particularly true for the fluxes list in the FIRST catalog we used here, which are obtained by fitting the sources usually as extended radio sources (cf. the ‘Deconv.MajAx’ column in the catalog). While it is difficult

---

<sup>9</sup>The VLA FIRST aims to produce Faint Image of the Radio Sky at Twenty centimeters using Very Large Array, which is operated by the National Radio Astronomy Observatory.

<sup>10</sup>Note that  $\sim 30$  sources are not covered by the FIRST, thus their upper limits are not calculated.

to seek clues from the radio morphology since most of these sources have very weak radio emissions ( $S_{20cm} < \sim 5$  mJy, close to the detection limit of 1 mJy), and their FIRST images are unresolved. Only one brighter object ( $S_{20cm} > 10$  mJy), SDSS J122412.51+160012.1, probably shows marginally extended structure with integrated to peak flux ratio of 1.5 and deconvolved major axis =  $5.45''$ . On the other hand, radio luminosities at 6 GHz may provide some information on the radio origins. It is suggested that for AGNs at low redshifts, low-luminosity radio emission with  $L_{6GHz} < 10^{23}$  W Hz $^{-1}$  seems to be powered by star formation, while that with  $L_{6GHz} \geq 10^{23}$  W Hz $^{-1}$  is more likely AGN-dominated (e.g., [Kimball et al. 2011](#); [Condon et al. 2013](#); [Kellermann et al. 2016](#)). The luminosity at 6 GHz is derived assuming a spectral slope of 0.46. All the objects except one (SDSS J122412.51+160012.1) have 6 GHz luminosities located in the range of  $10^{21}$  W Hz $^{-1} \leq L_{6GHz} \leq 10^{23}$  W Hz $^{-1}$ , and thus their radio fluxes may also be contributed from host stellar processes.

#### 4.4. Comparison with NLS1s

Most low-mass AGNs tend to have broad line widths (FWHMs) narrower than  $\sim 2000$  km/s, which is the conventional criterion of narrow-line Seyfert 1 galaxies (NLS1s; [Osterbrock & Pogge 1985](#)). It is thus interesting to compare these two AGN sub-classes. In fact, some objects in our total sample have also been classified as NLS1s in a comprehensive study of NLS1 AGNs from the SDSS DR3 by [Zhou et al. \(2006\)](#). NLS1s are characterized by some peculiar properties including the strong Fe II lines, weak [O III]/H $\beta$  line ratios, high Eddington ratios, low radio loud fraction, significant soft X-ray excess (in some), strong X-ray variability and steep X-ray spectra (see, e.g., [Laor 2000](#); [Komossa 2008](#), for reviews). Based simply on the BH mass estimation method from the line width and luminosity, a relative narrow broad line width can result from either a low black hole mass, or/and a high Eddington ratio. With their peculiar multi-wavelength properties, NLS1s are found to cluster at one end of the so-called EV1 which are suggested to be driven by high accretion rates ([Boroson & Green 1992](#)). Thus NLS1s are generally suggested to harbor relatively less massive black holes radiating near their Eddington limits.

However, LMBHs are selected only from black hole masses regardless the Eddington ratios. They are simply the low-BH-mass counterparts of classical Seyfert galaxies, and are expected to exhibit diverse properties depending on the Eddington ratios, which span a wide dynamical range. [Greene & Ho \(2004\)](#) found that their low-mass AGNs span a larger range in both the Fe II and the [O III] strengths relative to H $\beta$  than classical NLS1s. There is a wide distribution of the Eddington ratios in our sample, some as low as two orders of magnitudes below their Eddington limits. LMBHs show diverse properties in X-ray, with a wide range of the X-ray photon indices (e.g.  $\Gamma = 1.0\text{--}2.7$  in [Desroches et al. 2009](#);  $\Gamma = 1.5\text{--}2.8$  in [Dong R. et al. 2012](#) and  $\Gamma = 1.2\text{--}4.0$  in the

soft X-ray band for our sample). Moreover, some LMBHs, especially those with low Eddington ratios, do not show soft X-ray excess, as found in the spectrum of NGC 4395. On the other hand, some typical NLS1s, as those with extremely narrow widths of the broad lines as studied by [Ai et al. \(2011\)](#), do have BH masses as low as  $10^6 M_{\text{BH}}$  or below.

It is clear that NLS1s, when solely selected from the line width, are a heterogeneous class of AGNs which may include ordinary Seyfert galaxies having simply LMBHs, regardless the Eddington ratios. Classical NLS1s were selected by also considering the strong Fe II and weak [O III] emissions. These tend to select objects with high Eddington ratios given the observed Eigenvector I correlations. We thus suggest that a simple criterion based solely on the line width may not be a good approach for the selection of NLS1s and other criteria have to be incorporated. Similar remarks can also be found in [Ai et al. \(2011\)](#).

One interesting feature is that both types have relatively low fraction of radio-loud objects. This might be related to the suggested observed statistical relations among radio loudness, BH mass and Eddington ratio. However, the underlying physical mechanisms driving these relations are not known.

## 5. HOST GALAXY PROPERTIES

In this section, we briefly discuss on the properties of the host galaxies for the LMBHs and the possible co-evolution with BHs by making use of the SDSS data.

### 5.1. Luminosities, Colors and Morphologies

The host galaxy luminosities are calculated in a way following Dong+12 and GH07. First, the AGN luminosities are estimated from the broad  $H\alpha$  luminosities<sup>11</sup> that are free from starlight contamination, and are then subtracted from the SDSS photometric Petrosian  $g$ -band magnitude. The host galaxy luminosities are then derived after  $K$ -corrections using the routine of [Blanton & Roweis \(2007\)](#). The distributions of the  $g$ -band absolute magnitudes of AGN, host and the total are shown in Figure 12, with those in Dong+12 and GH07 plotted for comparison. The distributions of these luminosities for the DR7 LMBH sample are similar to those in Dong+12. The current sample has a median AGN luminosity of  $M_g = -17.80$  mag and a median host galaxy luminosity of  $M_g = -20.14$  mag (these values are  $-17.70$  and  $-20.22$  respectively in Dong+12). The median

---

<sup>11</sup> Assuming an optical spectral shape of 1.56 ( $f_\lambda \propto \lambda^{-1.56}$ ; [Vanden Berk et al. 2001](#)), we obtain the AGN luminosities using the scaling relation between  $L_{H\alpha^B}$  and  $\lambda L_\lambda(5100 \text{ \AA})$  described in [Greene & Ho \(2005\)](#).

host galaxy luminosity is slightly brighter than the characteristic luminosity of  $M_g^* = -20.1$  mag at  $z = 0.1$  (Blanton et al. 2003). Only 6 objects have host galaxy luminosities falling into the dwarf galaxy of  $M_g > -18.0$  mag. It indicates that although LMBHs usually indeed reside in small stellar systems, their hosts may not necessarily be dominantly dwarf galaxies. Note that the host galaxy luminosities are possibly overestimated in our AGN-host separation method since the fiber loss may result in underestimation of the nuclear luminosity, though the systematic overestimation is smaller than 0.3 mag according to GH07. Furthermore, the AGN luminosities estimated from the  $H\alpha$  luminosities assuming a power-law continuum may be subject to an uncertainty of about 0.1 mag (Dong+12).

In general, it is not practical to visually classify the galaxy morphology for most of our sample objects using the SDSS images due to their limited depth and spatial resolution. Instead we try to gain information on the morphologies from the host galaxy colors. The  $u - g$  colors are found to have a mean value of 1.28 mag with a standard deviation of 0.38 mag, and the  $g - r$  colors have a mean of 0.61 mag and a standard deviation of 0.16 mag. They correspond to the typical colors of Sbc galaxies according to Fukugita et al. (1995).

## 5.2. Stellar Populations

Two stellar indices, the 4000 Å break strength ( $D_{4000}$ ) and Balmer absorption line index ( $H\delta_A$ ) are used to infer the stellar populations of the host galaxies. In general,  $D_{4000}$  is small for young stellar populations ( $D_{4000} < 1.5$  for ages  $< 1$  Gyr) and large for old, metal-rich galaxies. On the other hand, galaxies having experienced star burst activity that has ended  $\sim 0.1-1$  Gyr ago tend to show strong  $H\delta$  absorption lines (Kauffmann et al. 2003a). Hence these two indices can be used to constrain the mean stellar ages of the host galaxies of LMBHs and to diagnose the star formation history over the past few Gyrs.

The two indices are calculated from the decomposed stellar component as described in Section 2.1 based on the definition and calculation method in Kauffmann et al. (2003a). Note that only 157 objects with the AGN contribution less than 75% at 4000 Å in the SDSS spectra are used. The resulting typical errors ( $1 \sigma$ ) of the two indices for the LMBH sample are 0.1 and 1.6, respectively (see Section 4.2.3 in Dong+12 for the details of error estimation).

The distribution of 419 low-mass AGNs (262 objects in Dong+12 also included) on the  $D_{4000}-H\delta_A$  plane is shown in Figure 13, and the distribution of  $\sim 492,000$  inactive galaxies is plotted as contours for comparison. These inactive galaxies are derived from the SDSS DR7 classified as “galaxies” by the SDSS pipeline and with  $S/N > 5 \text{ pixel}^{-1}$  around 4000 Å in their spectra. In addition, broad-line AGNs and those Seyfert 2 galaxies defined by the BPT diagram are excluded.

Note that the negative values of  $H\delta_A$  are due to the definition and corresponding calculation method of the line index (Kauffmann et al. 2003a; Worthey & Ottaviani 1997). Most of our LMBH hosts (112 out of 157) have  $D_{4000} < 1.5$  indicating that their mean stellar ages tend to be less than 1 Gyr. In general, for those galaxies with  $D_{4000} < 1.5$ , if they have experienced instantaneous burst of star formation in the last few Gyrs, they tend to have  $H\delta_A > 5$ . However, most objects with  $D_{4000} < 1.5$  in our LMBH sample do not follow this tendency. It indicates that the distribution of our LMBHs on the  $D_{4000}$ – $H\delta_A$  plane is more likely overlapping the locus of continuous star formation, which is in broad agreement with that of normal galaxies.

Studies of optical images and spectra indicated that there are two distinct populations of the host galaxies of the LMBHs (Greene et al. 2008; Jiang et al. 2011). The major are gas-rich, late-type galaxies similar to the prototypal NGC 4395. The rest are spheroidal galaxies like POX 52 which has deficient gas and red color. Kormendy & Bender (2012) suggested that such spheroidal galaxies were transformed from irregular and late-type disk galaxies at an early epoch, by both internal and secular processes. The low fraction of LMBH host galaxies with nearby companions also imply these galaxies mainly evolve through secular processes (Jiang et al. 2011). This is also supported by the above finding that most of the host galaxies of our LMBHs undergo continuous star formation in the past few Gyrs.

### 5.3. Stellar Masses

The stellar masses of the host galaxies are estimated using three methods. The first is by using Near-infrared (NIR) photometry which can be considered as a tracer of stellar mass. In the NIR band, the luminosities of the LMBH AGNs are dominated by host galaxies, and AGNs have negligible contribution ( $\sim 7\%$ <sup>12</sup>). Moreover, the mass-to-light ratio in the NIR band is sensitive neither to dust absorption nor to star formation history. Of the total sample, 180 objects are detected in the Two-Micron All-Sky Survey (2MASS<sup>13</sup>) and among the rest, 129 objects are detected in the UKIRT Infrared Deep Sky Surveys (UKIDSS; Lawrence et al. 2007). Here we adopt the mass-to-light ratios provided by Into & Portinari (2013, the scatter is about 0.1 dex), which are dependent

---

<sup>12</sup>We simply estimate the AGN contribution in the K-band using the relative flux ratio between 5100 Å and 2.2 micron from the mean nuclear spectral energy distribution (SED) of the nearest Seyfert 1 galaxies (Prieto et al. 2010) that includes the AGN continuum and torus emission in the NIR band. The flux at 5100 Å is derived from  $L_{H\alpha^B}$  (Greene & Ho 2005).

<sup>13</sup>Our LMBHs tend to be extended sources since they are mostly located in the low-redshift universe. Thus the result is derived by cross-matching the LMBH sample with 2MASS All-Sky Extended Source Catalog (XSC).

on the galaxy colors  $r - i$ ,

$$\log(M_*/L_{Ks}) = 2.843(r - i) - 1.093, \quad (3)$$

where  $L_{Ks}$  is the Ks-band luminosity from 2MASS in units of  $L_\odot$ , and  $r - i$  is the color derived from the SDSS Petrosian magnitudes after  $K$ -correction and subtraction of the AGN continuum. The  $K$ -correction is calculated following Blanton & Roweis (2007). The K-band magnitudes of the UKIDSS-detected sources are transformed to the 2MASS Ks-band using the color equations given by Hewett et al. (2006). For the sources not detected in 2MASS and UKIDSS, we derive their stellar masses from the MPA–JHU catalog<sup>14</sup> (Kauffmann et al. 2003b; Brinchmann et al. 2004; Tremonti et al. 2004; Salim et al. 2007) if available, or otherwise using the relation between  $M_*$  and the  $3.4 \mu\text{m}$  luminosity from the Wide-field Infrared Survey Explorer (WISE) All-Sky survey calibrated using the MPA–JHU catalog (Wen et al. 2013). We compare the stellar masses given by the MPA–JHU catalog with those derived from the NIR luminosities and  $r - i$  colors for those objects detected in both surveys, and found that the two estimators are statistically in good agreement. The stellar masses for the total sample range from  $6.0 \times 10^8 M_\odot$  to  $2.5 \times 10^{12} M_\odot$ , with a median of  $3.7 \times 10^{10} M_\odot$ , slightly lower than that of the MPA–JHU sample ( $5.7 \times 10^{10} M_\odot$ , see Figure 14 for their distributions). The stellar masses are mostly greater than  $10^{9.5} M_\odot$ , which is the mass of the Large Magellanic Cloud (LMC), indicating again that LMBHs do not necessarily reside in dwarf galaxies.

The 512 sources with reliable stellar mass estimations are plotted on the color–mass diagram (see Figure 15). The green lines indicate the location of the so-called green valley defined by Schawinski et al. (2014), which is a superposition of red and blue galaxies with the same intermediate optical colors. It has been suggested to be a special stage in the evolution of massive galaxies after star formation is quenched, and perhaps as an evidence of AGN feedback. Our LMBH sources span almost the entire  $u - r$  color range, while most are located in the green valley or blue sequence, which is consistent with the suggestion that most low-mass AGNs in GH07 reside in gas-rich, disk galaxies (Jiang et al. 2011).

We note that there still exist about 11% of our sample objects in the red sequence. An inter-

---

<sup>14</sup>The MPA–JHU catalog, which contains properties of millions of galaxies from the SDSS DR7, was produced by a collaboration of researchers from the Max Planck Institute for Astrophysics (MPA) and the Johns Hopkins University (JHU). It contains two subsets, the raw data and the derived data. The raw data contain spectral parameters including the line fluxes, equivalent widths and continuum indices, as well as basic information about the objects such as their redshifts, velocity dispersions and plate, fiber and MJD. The derived data include gas-phase metallicities, star formation rates and stellar masses. The stellar masses are calculated from fits to the photometry with population synthesis models following the philosophy of Kauffmann et al. (2003b) and Salim et al. (2007). In this study we use the improved version of stellar mass catalog which can be obtained from <http://home.strw.leidenuniv.nl/~jarle/SDSS/>.

esting question arises: How were these LMBH AGNs triggered and fueled in such red and presumably gas-deficit galaxies? We know that AGN activity requires both available feeding fuel (gas or stars), and a process to get out of their angular momentum. As discussed in [Kormendy & Ho \(2013\)](#), the feeding rates of low-mass AGNs are very modest. Assuming these LMBHs accrete at their Eddington limits, the mass accretion rate  $\dot{M} = 2.2 \times 10^{-8} (\eta/0.1) (M_{\text{BH}}/M_{\odot}) M_{\odot}$ , is only  $\sim 0.02 M_{\odot}/\text{year}$  for BHs with  $M_{\text{BH}} \sim 10^6 M_{\odot}$  ([Kormendy & Ho 2013](#)). These values are tiny even for red galaxies and hence there may always be enough gas to feed the nuclear low-mass AGNs. On the other hand, various physical process may break the “angular momentum barrier” and push the gas into the nuclear regions of galaxies such as wet major and minor mergers of the galaxies (e.g., [Silk & Rees 1998](#); [Hopkins et al. 2008](#)), inflow along spiral arms or bar (for instance, NGC 1097; e.g., [Davies et al. 2009](#); [Fathi et al. 2006](#)) and disk instabilities (e.g., cold flows; [Dekel et al. 2009](#); [Bournaud et al. 2011](#)). Current observations show evidence that the triggering of low-mass AGNs are indeed dominated by secular processes. For instance, about 90% of the LMBH AGNs in the low-redshift universe reside in galaxies with the so-called pseudobulges which are formed mainly by slow process without major mergers involved ([Jiang et al. 2011](#)). Our result on the  $D_{4000}\text{--}H\delta_A$  distribution also support this idea. The other processes, however, may not be completely ruled out. For example, SDSS J083803.68+540642.0, a red and gas-poor LINER in the sample of Dong+12, shows a peculiar circumgalactic ring, which may be caused by collision with a gas-rich galaxy, suggesting history of violent galaxy interaction ([Liu et al. 2017](#)). Such a process may also play a role in triggering low-mass AGN. As discussed in [Liu et al. \(2017\)](#), major mergers of low-mass galaxies in the local universe may be more common than massive galaxies. Further studies are needed to fully understand this question.

#### 5.4. Co-evolution of LMBHs and Their Host Galaxies?

As discussed above, LMBHs seem to evolve with secular processes and have not experienced major mergers. Thus they can be used to trace the initial stage of the evolution of BHs and their host galaxies. We briefly investigate the co-evolution between BHs and host galaxies in the low-mass regime by using the relation between BH mass accretion rates and host star formation rates (SFRs). The mass accretion rates are derived from the bolometric luminosities assuming the efficiency factor  $\eta = 0.1$ , while the SFRs are given by the MPA–JHU catalog with no aperture corrections. [Figure 16](#) shows the distribution of 282 low-mass AGNs with both quantities available on the diagram of mass accretion rates versus SFRs, revealing a strong correlation between them.

This suggests that there may exist a connection between the AGN activity and the star formation. However, more compelling and direct evidence is still needed to support the co-evolution of LMBHs and their hosts. In fact, there is no strong evidence that LMBHs have direct feedback

on their host galaxies in the local universe. Furthermore, the link between BH accretion and star formation may also be explained by that they both depend on the gas from the same reservoir (Kormendy & Kennicutt 2004). Nevertheless, our result hints at a possible co-evolution scenario between LMBHs and their host galaxies.

## 6. SUMMARY

Using the optical spectrometric data from the SDSS DR7, we obtain a sample of 204 new AGNs with low-mass black holes, and expand the SDSS LMBH sample from the DR4 (Dong+12) to a total of 513 objects. This is the largest optically selected, broad line low-mass AGN sample so far. The BH masses, estimated using the virial method, are in the range of  $1.1 \times 10^5$  to  $2.0 \times 10^6 M_\odot$ , with a median of  $1.3 \times 10^6 M_\odot$ . The Eddington ratios range from 0.01 to 2, with a median of 0.26. The properties and distributions of the new sample are statistically consistent with those of Dong+12.

We present some statistical properties of the combined LMBH AGN sample from this work and Dong+12, focusing on the emission lines and multi-wavelength properties including X-ray and radio, as well as their host galaxies. Most of the LMBHs are located in the Seyfert galaxy and composite regions on the narrow-line diagnostic diagrams, confirming their AGN nature. 102 sources were detected by *ROSAT*. LMBHs with X-ray detections tend to follow the correlation between the X-ray luminosities (2–10 keV) and [O III]  $\lambda 5007$  luminosities derived from more massive AGNs. The optical/X-ray effective indices  $\alpha_{\text{OX}}$  of X-ray detected AGNs show a large scatter ranging from  $-1.58$  to  $-0.70$ , and are systematically flatter than more massive AGNs. In general, they are broadly consistent with the extrapolation of the  $\alpha_{\text{OX}}-L_{2500\text{\AA}}$  relation to the low-luminosity end. No dependence of  $\alpha_{\text{OX}}$  is found on  $L_{\text{bol}}/L_{\text{Edd}}$ , whereas a weak correlation between  $\alpha_{\text{OX}}$  and  $M_{\text{BH}}$  is suggested, which is consistent with Dong R. et al. (2012). Only 5% of the sources are detected in the FIRST survey, which are mostly radio loud. Thus we suggest that LMBHs are predominately radio-quiet, though further deep radio observations are needed to confirm this result.

The host galaxies of LMBHs have  $g$ -band magnitudes ( $M_g$ ) ranging from  $-22.2$  to  $-15.9$  mag, with a median comparable to the characteristic luminosity of  $M_g^* = -20.1$  mag at  $z = 0.1$ . The colors of the galaxies suggest mostly a type of typical Sbc in general. The galaxies have stellar masses ( $M_*$ ) ranging from  $10^{8.8}$  to  $10^{12.4} M_\odot$ , with a median of  $10^{10.6} M_\odot$ , which is slightly lower than that of the SDSS DR7 sample from the MPA–JHU catalog. Only a few tens have  $M_* < 10^{10} M_\odot$  or  $M_g > -18$  mag. Thus low-mass BHs may live in lower-mass stellar systems, but do not necessarily reside in the dwarf galaxies. Most of the galaxies have mean stellar ages younger than 1 Gyr from their  $D_{4000}$  values. The locus on the  $D_{4000}-\text{H}\delta_{\text{A}}$  diagram indicates that they tend to have experienced continuous star formation over the past few Gyrs, which is consistent with the

suggestion that their host galaxies of LMBHs mainly evolve via secular processes (e.g., [Jiang et al. 2011](#); [Kormendy & Ho 2013](#)). Their distribution on the color versus  $M_*$  diagram shows that most of these are blue, late-type galaxies.

With homogeneous selection and accurately measurements of the spectral parameters, our SDSS LMBH sample provides a useful database to further explore the properties of low-mass BHs and their host galaxies, as well as to study the BH mass function in the low-mass regime.

This work is supported by the National Natural Science Foundation of China (grant No. 11473035 and No. 11473062) and the National Program on Key Research and Development Project (Grant No. 2016YFA0400804). W.L. acknowledges supports from the Natural Science Foundation of China grant (NSFC 11703079) and the “Light of West China” Program of Chinese Academy of Sciences (CAS). H.L. thanks NAOC for providing the computing resources on Zen cluster. We are grateful to the anonymous referee for his/her constructive comments that improved the paper. This work is mainly based on the observations obtained by the SDSS, we acknowledge the entire SDSS team for providing the data that made this work possible. We have made use of the *ROSAT* Data Archive of the Max-Planck-Institut für extraterrestrische Physik (MPE) at Garching, Germany. This publication also makes use of data products from the Wide-field Infrared Survey Explorer (WISE) and the Two Micron All Sky Survey (2MASS). WISE is a joint project of the University of California, Los Angeles, and the Jet Propulsion Laboratory/California Institute of Technology, which are funded by the National Aeronautics and Space Administration (NASA). 2MASS is a joint project of the University of Massachusetts and the Infrared Processing and Analysis Center/California Institute of Technology, funded by the NASA and the National Science Foundation (NSF). We also use the data from the UKIDSS, which uses the UKIRT Wide Field Camera.

## REFERENCES

- Abazajian, K. N., Adelman-McCarthy, J. K., Agüeros, M. A., et al. 2009, *ApJS*, 182, 543
- Abbott, B. P., Abbott, R., Abbott, T. D., et al. 2016, *Physical Review Letters*, 116, 061102
- Adelman-McCarthy, J. K., Agüeros, M. A., Allam, S. S., et al. 2006, *ApJS*, 162, 38
- Ai, Y. L., Yuan, W., Zhou, H. Y., Wang, T. G., & Zhang, S. H. 2011, *ApJ*, 727, 31
- Avni, Y., & Tananbaum, H. 1986, *ApJ*, 305, 83
- Baldwin, J. A., Phillips, M. M., & Terlevich, R. 1981, *PASP*, 93, 5
- Barth, A. J., Greene, J. E., & Ho, L. C. 2008, *AJ*, 136, 1179

- Barth, A. J., Ho, L. C., Rutledge, R. E., & Sargent, W. L. W. 2004, *ApJ*, 607, 90
- Barth, A. J., Sarzi, M., Rix, H.-W., et al. 2001, *ApJ*, 555, 685
- Becker, R. H., White, R. L., & Helfand, D. J. 1995, *ApJ*, 450, 559
- Bentz, M. C., Peterson, B. M., Netzer, H., Pogge, R. W., & Vestergaard, M. 2009, *ApJ*, 697, 160
- Bentz, M. C., Peterson, B. M., Pogge, R. W., Vestergaard, M., & Onken, C. A. 2006, *ApJ*, 644, 133
- Bentz, M. C., Denney, K. D., Grier, C. J., et al. 2013, *ApJ*, 767, 149
- Best, P. N., Kauffmann, G., Heckman, T. M., et al. 2005, *MNRAS*, 362, 25
- Blanton, M. R., & Roweis, S. 2007, *AJ*, 133, 734
- Blanton, M. R., Hogg, D. W., Bahcall, N. A., et al. 2003, *ApJ*, 592, 819
- Boller, T., Freyberg, M. J., Trümper, J., et al. 2016, *A&A*, 588, A103
- Boroson, T. A., & Green, R. F. 1992, *ApJS*, 80, 109
- Bournaud, F., Dekel, A., Teyssier, R., et al. 2011, *ApJ*, 741, L33
- Brinchmann, J., Charlot, S., White, S. D. M., et al. 2004, *MNRAS*, 351, 1151
- Bruzual, G., & Charlot, S. 2003, *MNRAS*, 344, 1000
- Condon, J. J., Kellermann, K. I., Kimball, A. E., Ivezić, Ž., & Perley, R. A. 2013, *ApJ*, 768, 37
- Conselice, C. J., Bluck, A. F. L., Mortlock, A., Palamara, D., & Benson, A. J. 2014, *MNRAS*, 444, 1125
- Davies, R. I., Maciejewski, W., Hicks, E. K. S., et al. 2009, *ApJ*, 702, 114
- Dekel, A., Birnboim, Y., Engel, G., et al. 2009, *Nature*, 457, 451
- Desroches, L.-B., Greene, J. E., & Ho, L. C. 2009, *ApJ*, 698, 1515
- Dewangan, G. C., Mathur, S., Griffiths, R. E., & Rao, A. R. 2008, *ApJ*, 689, 762
- Dickey, J. M., & Lockman, F. J. 1990, *ARA&A*, 28, 215
- Dong, X., Wang, T., Wang, J., et al. 2008, *MNRAS*, 383, 581
- Dong, X., Wang, T., Yuan, W., et al. 2007, *ApJ*, 657, 700

- Dong, X.-B., Ho, L. C., Yuan, W., et al. 2012, *ApJ*, 755, 167 (Dong+12)
- Dong, X.-B., Wang, J.-G., Ho, L. C., et al. 2011, *ApJ*, 736, 86
- Dong R., Greene, J. E., & Ho, L. C. 2012, *ApJ*, 761, 73
- Fathi, K., Storchi-Bergmann, T., Riffel, R. A., et al. 2006, *ApJ*, 641, L25
- Ferrarese, L., & Merritt, D. 2000, *ApJ*, 539, L9
- Filippenko, A. V., & Ho, L. C. 2003, *ApJ*, 588, L13
- Fitzpatrick, E. L. 1999, *PASP*, 111, 63
- Fukugita, M., Ichikawa, T., Gunn, J. E., et al. 1996, *AJ*, 111, 1748
- Fukugita, M., Shimasaku, K., & Ichikawa, T. 1995, *PASP*, 107, 945
- Gebhardt, K., Bender, R., Bower, G., et al. 2000a, *ApJ*, 539, L13
- Gebhardt, K., Kormendy, J., Ho, L. C., et al. 2000b, *ApJ*, 543, L5
- Ghez, A. M., Salim, S., Weinberg, N. N., et al. 2008, *ApJ*, 689, 1044
- Greene, J. E. 2012, *Nature Communications*, 3, 1304
- Greene, J. E., & Ho, L. C. 2004, *ApJ*, 610, 722
- . 2005, *ApJ*, 630, 122
- . 2006, *ApJ*, 641, L21
- . 2007a, *ApJ*, 670, 92 (GH07)
- . 2007b, *ApJ*, 656, 84
- Greene, J. E., Ho, L. C., & Barth, A. J. 2008, *ApJ*, 688, 159
- Grier, C. J., Martini, P., Watson, L. C., et al. 2013, *ApJ*, 773, 90
- Gültekin, K., Richstone, D. O., Gebhardt, K., et al. 2009, *ApJ*, 698, 198
- Gunn, J. E., Carr, M., Rockosi, C., et al. 1998, *AJ*, 116, 3040
- Gunn, J. E., Siegmund, W. A., Mannery, E. J., et al. 2006, *AJ*, 131, 2332
- Hao, L., Strauss, M. A., Tremonti, C. A., et al. 2005, *AJ*, 129, 1783

- Heckman, T. M. 1980, *A&A*, 87, 152
- Ho, L. C. 2009, *ApJ*, 699, 626
- Ho, L. C., Filippenko, A. V., & Sargent, W. L. W. 1997a, *ApJS*, 112, 315
- . 1997b, *ApJ*, 487, 568
- Ho, L. C., & Peng, C. Y. 2001, *ApJ*, 555, 650
- Hopkins, P. F., Hernquist, L., Cox, T. J., & Kereš, D. 2008, *ApJS*, 175, 356
- Hughes, S. A. 2002, *MNRAS*, 331, 805
- Into, T., & Portinari, L. 2013, *MNRAS*, 430, 2715
- Ivezić, Ž., Menou, K., Knapp, G. R., et al. 2002, *AJ*, 124, 2364
- Iwasawa, K., Fabian, A. C., Almaini, O., et al. 2000, *MNRAS*, 318, 879
- Jiang, Y.-F., Greene, J. E., Ho, L. C., Xiao, T., & Barth, A. J. 2011, *ApJ*, 742, 68
- Jin, C., Ward, M., & Done, C. 2012, *MNRAS*, 425, 907
- Just, D. W., Brandt, W. N., Shemmer, O., et al. 2007, *ApJ*, 665, 1004
- Kaaret, P., Feng, H., & Roberts, T. P. 2017, *ARA&A*, 55, 303
- Kaspi, S., Maoz, D., Netzer, H., et al. 2005, *ApJ*, 629, 61
- Kauffmann, G., Heckman, T. M., White, S. D. M., et al. 2003a, *MNRAS*, 341, 33
- Kauffmann, G., Heckman, T. M., Tremonti, C., et al. 2003b, *MNRAS*, 346, 1055
- Kellermann, K. I., Condon, J. J., Kimball, A. E., Perley, R. A., & Ivezić, Ž. 2016, *ApJ*, 831, 168
- Kelly, B. C., Treu, T., Malkan, M., Pancoast, A., & Woo, J.-H. 2013, *ApJ*, 779, 187
- Kewley, L. J., Dopita, M. A., Sutherland, R. S., Heisler, C. A., & Trevena, J. 2001, *ApJ*, 556, 121
- Kewley, L. J., Groves, B., Kauffmann, G., & Heckman, T. 2006, *MNRAS*, 372, 961
- Kimball, A. E., Kellermann, K. I., Condon, J. J., Ivezić, Ž., & Perley, R. A. 2011, *ApJ*, 739, L29
- Komossa, S. 2008, in *Revista Mexicana de Astronomia y Astrofisica Conference Series*, Vol. 32, *Revista Mexicana de Astronomia y Astrofisica Conference Series*, 86–92

- Kormendy, J., & Bender, R. 2012, *ApJS*, 198, 2
- Kormendy, J., & Ho, L. C. 2013, *ARA&A*, 51, 511
- Kormendy, J., & Kennicutt, Jr., R. C. 2004, *ARA&A*, 42, 603
- Laor, A. 2000, *New A Rev.*, 44, 503
- Lawrence, A., Warren, S. J., Almaini, O., et al. 2007, *MNRAS*, 379, 1599
- Liu, B. F., Mineshige, S., & Ohsuga, K. 2003, *ApJ*, 587, 571
- Liu, W.-J., Qian, L., Dong, X.-B., et al. 2017, *ApJ*, 837, 109
- Lodato, G., & Natarajan, P. 2006, *MNRAS*, 371, 1813
- Lu, H., Zhou, H., Wang, J., et al. 2006, *AJ*, 131, 790
- Ludlam, R. M., Cackett, E. M., Gültekin, K., et al. 2015, *MNRAS*, 447, 2112
- Magorrian, J., Tremaine, S., Richstone, D., et al. 1998, *AJ*, 115, 2285
- McLure, R. J., & Dunlop, J. S. 2004, *MNRAS*, 352, 1390
- Miniutti, G., Ponti, G., Greene, J. E., et al. 2009, *MNRAS*, 394, 443
- Moran, E. C., Eracleous, M., Leighly, K. M., et al. 2005, *AJ*, 129, 2108
- Moran, E. C., Shahinyan, K., Sugarman, H. R., Vélez, D. O., & Eracleous, M. 2014, *AJ*, 148, 136
- Narayan, R., & Yi, I. 1995, *ApJ*, 452, 710
- Osterbrock, D. E., & Pogge, R. W. 1985, *ApJ*, 297, 166
- Pan, H.-W., Yuan, W., Zhou, X.-L., Dong, X.-B., & Liu, B. 2015, *ApJ*, 808, 163
- Panessa, F., Bassani, L., Cappi, M., et al. 2006, *A&A*, 455, 173
- Peterson, B. M., Bentz, M. C., Desroches, L.-B., et al. 2005, *ApJ*, 632, 799
- Plotkin, R. M., Gallo, E., Haardt, F., et al. 2016, *ApJ*, 825, 139
- Ponti, G., Papadakis, I., Bianchi, S., et al. 2012, *A&A*, 542, A83
- Prieto, M. A., Reunanen, J., Tristram, K. R. W., et al. 2010, *MNRAS*, 402, 724
- Reines, A. E., Greene, J. E., & Geha, M. 2013, *ApJ*, 775, 116

- Richstone, D., Ajhar, E. A., Bender, R., et al. 1998, *Nature*, 395, A14
- Salim, S., Rich, R. M., Charlot, S., et al. 2007, *ApJS*, 173, 267
- Schartel, N., Green, P. J., Anderson, S. F., et al. 1996, *MNRAS*, 283, 1015
- Schawinski, K., Urry, C. M., Simmons, B. D., et al. 2014, *MNRAS*, 440, 889
- Schlegel, D. J., Finkbeiner, D. P., & Davis, M. 1998, *ApJ*, 500, 525
- Schulze, A., & Wisotzki, L. 2010, *A&A*, 516, A87
- Silk, J., & Rees, M. J. 1998, *A&A*, 331, L1
- Steffen, A. T., Strateva, I., Brandt, W. N., et al. 2006, *AJ*, 131, 2826
- Tananbaum, H., Avni, Y., Branduardi, G., et al. 1979, *ApJ*, 234, L9
- Thornton, C. E., Barth, A. J., Ho, L. C., Rutledge, R. E., & Greene, J. E. 2008, *ApJ*, 686, 892
- Tremonti, C. A., Heckman, T. M., Kauffmann, G., et al. 2004, *ApJ*, 613, 898
- Ulvestad, J. S., & Ho, L. C. 2001, *ApJ*, 558, 561
- Vanden Berk, D. E., Richards, G. T., Bauer, A., et al. 2001, *AJ*, 122, 549
- Veilleux, S., & Osterbrock, D. E. 1987, *ApJS*, 63, 295
- Véron-Cetty, M.-P., Joly, M., & Véron, P. 2004, *A&A*, 417, 515
- Vignali, C., Brandt, W. N., & Schneider, D. P. 2003, *AJ*, 125, 433
- Volonteri, M. 2010, *A&A Rev.*, 18, 279
- Volonteri, M., Lodato, G., & Natarajan, P. 2008, *MNRAS*, 383, 1079
- Volonteri, M., & Natarajan, P. 2009, *MNRAS*, 400, 1911
- Wen, X.-Q., Wu, H., Zhu, Y.-N., et al. 2013, *MNRAS*, 433, 2946
- White, R. L., Becker, R. H., Helfand, D. J., & Gregg, M. D. 1997, *ApJ*, 475, 479
- Worthey, G., & Ottaviani, D. L. 1997, *ApJS*, 111, 377
- Wrobel, J. M., & Ho, L. C. 2006, *ApJ*, 646, L95
- Wu, J., Vanden Berk, D., Grupe, D., et al. 2012, *ApJS*, 201, 10

- York, D. G., Adelman, J., Anderson, Jr., J. E., et al. 2000, *AJ*, 120, 1579
- Yuan, W., Brinkmann, W., Siebert, J., & Voges, W. 1998, *A&A*, 330, 108
- Yuan, W., Zhou, H., Dou, L., et al. 2014, *ApJ*, 782, 55
- Yuan, W., Zhou, H. Y., Komossa, S., et al. 2008, *ApJ*, 685, 801
- Zhou, H., Wang, T., Yuan, W., et al. 2006, *ApJS*, 166, 128

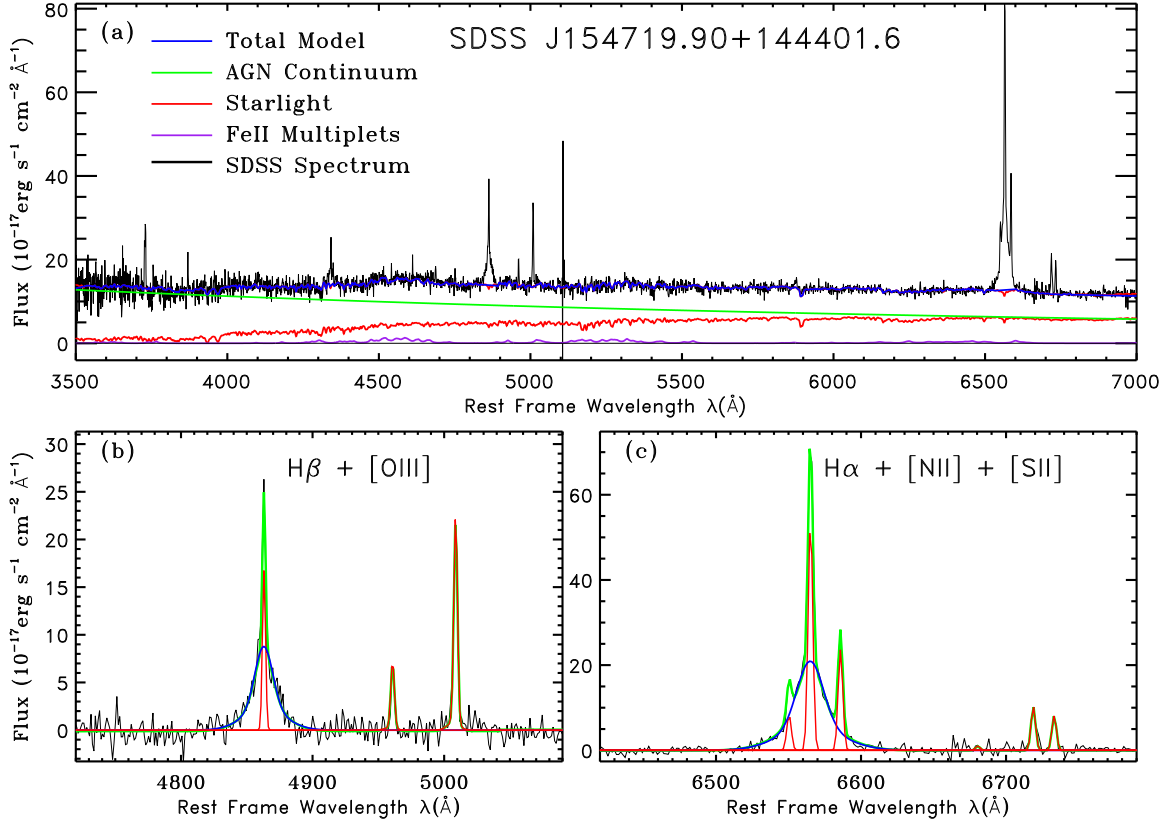


Fig. 1.— Illustration of the continuum and emission-line fitting for one of our LMBH AGNs as an example. Panel (a): The observed SDSS spectrum (black), the total model (blue), the decomposed components of the host galaxy (red), the AGN continuum (green), and the Fe II multiplets (purple). Panel (b): Emission-line profile fitting in the  $H\beta + [O III]$  region. Panel (c): Emission-line profile fitting in the  $H\alpha + [N II] + [S II]$  region. (The illustration of the continuum and emission-line fitting for all the LMBH AGNs are available in the online journal.)

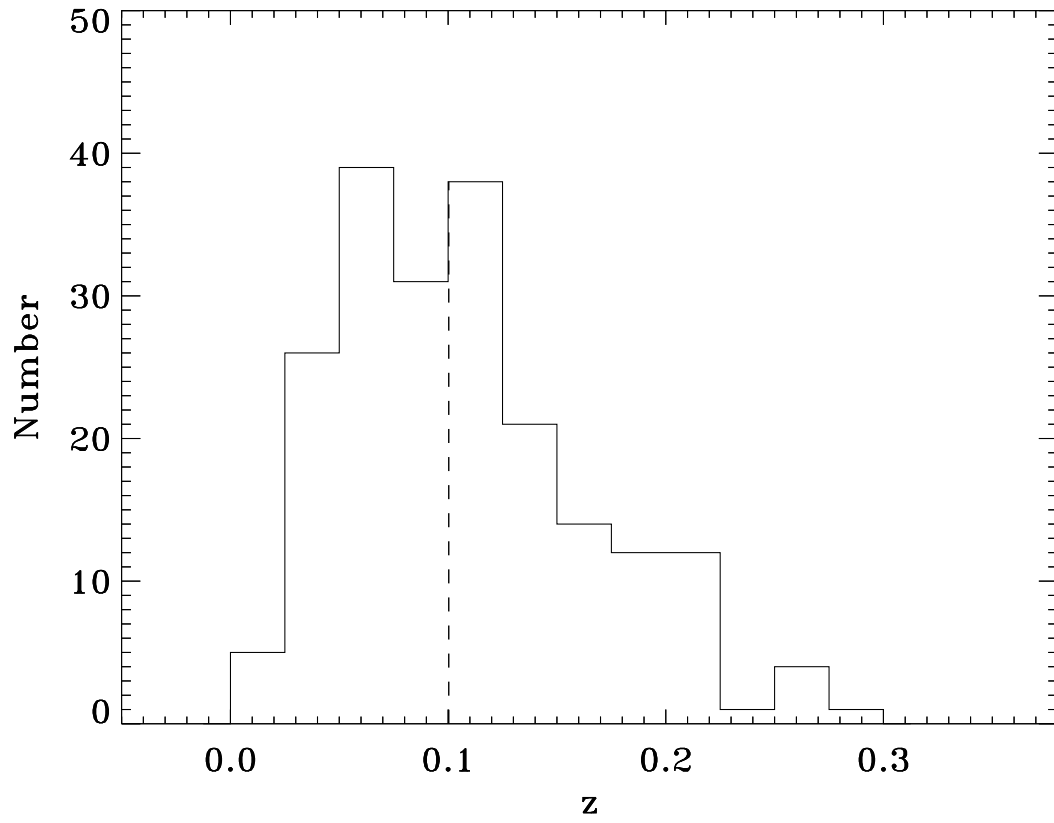


Fig. 2.— Redshift distribution for our 204 low-mass AGNs. The dashed line denotes the median.

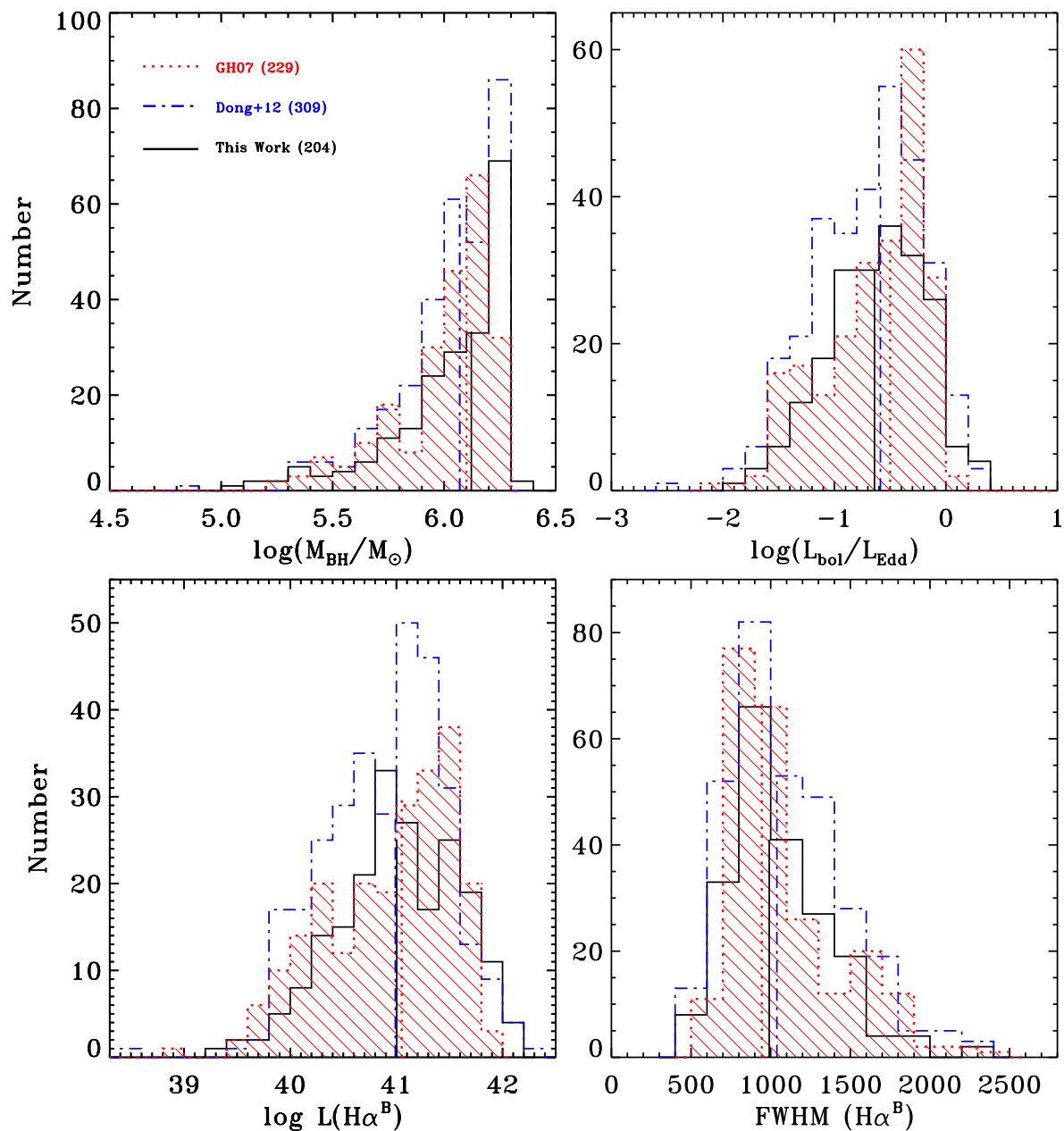


Fig. 3.— Distributions of the BH mass, Eddington ratio, luminosity and the FWHM of broad  $\text{H}\alpha$  for the LMBH sample in this work (black solid histograms), GH07 (red dotted histograms) and Dong+12 (blue dotted dashed histograms). The vertical lines denote the corresponding medians. Numbers in brackets of the upper left panel indicate the sample sizes.

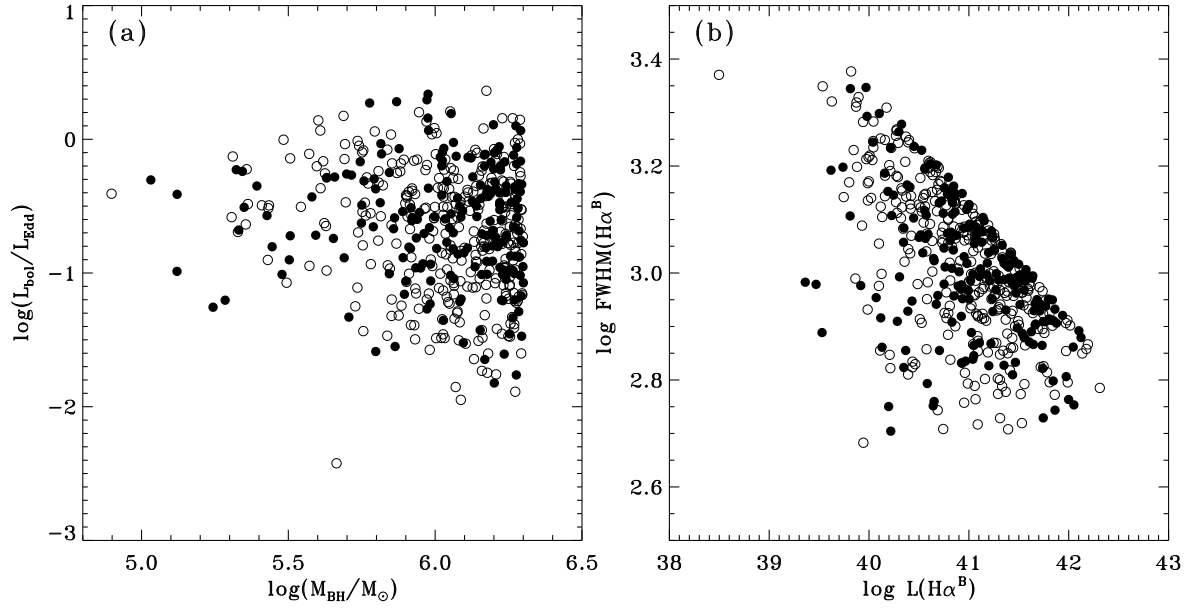


Fig. 4.— Distributions of the LMBH sample in this work (filled circles) and Dong+12 (open circles) on the  $L_{\text{bol}}/L_{\text{Edd}}$  versus  $M_{\text{BH}}$  plane (a) and on the  $\text{FWHM}_{\text{H}\alpha^{\text{B}}}$  versus  $L_{\text{H}\alpha^{\text{B}}}$  plane (b).

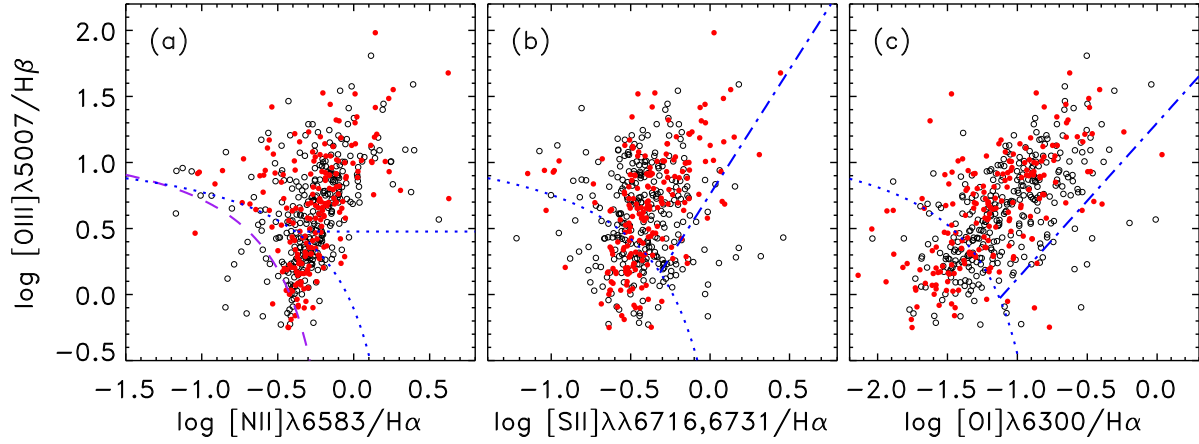


Fig. 5.— Narrow-line diagnostic diagrams of  $[O III] \lambda 5007 / H\beta$  versus  $[N II] \lambda 6583 / H\alpha$  (a), versus  $[S II] \lambda \lambda 6716, 6731 / H\alpha$  (b), and versus  $[O I] \lambda 6300 / H\alpha$  (c) for the LMBH sample in this study (black open circles) and Dong+12 sample (red filled circles). The extreme starburst classification line (blue dotted curve) from Kewley et al. (2001) and the Seyfert–LINER line (blue dotted dashed line) obtained by Kewley et al. (2006) are adopted to separate H II regions, AGNs and LINERs. In panel (a), the purple dashed line corresponds to the pure star formation line given by Kauffmann et al. (2003b), and the blue dotted horizontal line represents  $[O III] \lambda 5007 / H\beta = 3$ , which is conventionally used to separate Seyfert galaxies and LINERs.

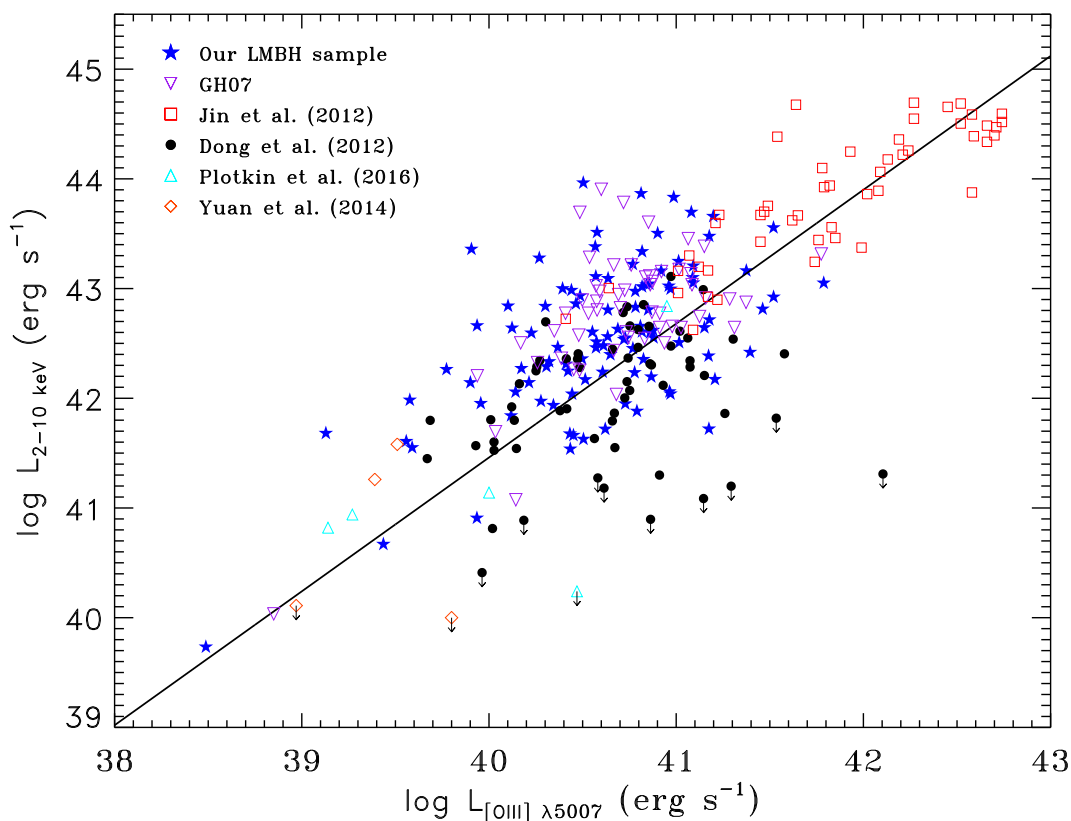


Fig. 6.— X-ray luminosity in 2–10 keV versus [O III]  $\lambda 5007$  luminosity for our total LMBH sample detected with *ROSAT* (blue filled star symbols), GH07 sample with *ROSAT* detections (purple open inverted triangles), LMBHs with *Chandra* detections in Dong R. et al. (2012, black filled circles), low-mass active galaxies with low Eddington ratios from Yuan et al. (2014, orange red open diamonds) and Plotkin et al. (2016, cyan open triangles), and more massive AGNs from Jin et al. (2012, red open squares). The black solid line represents the relation for Seyfert galaxies and QSOs given by Panessa et al. (2006). Arrows denote upper limits.

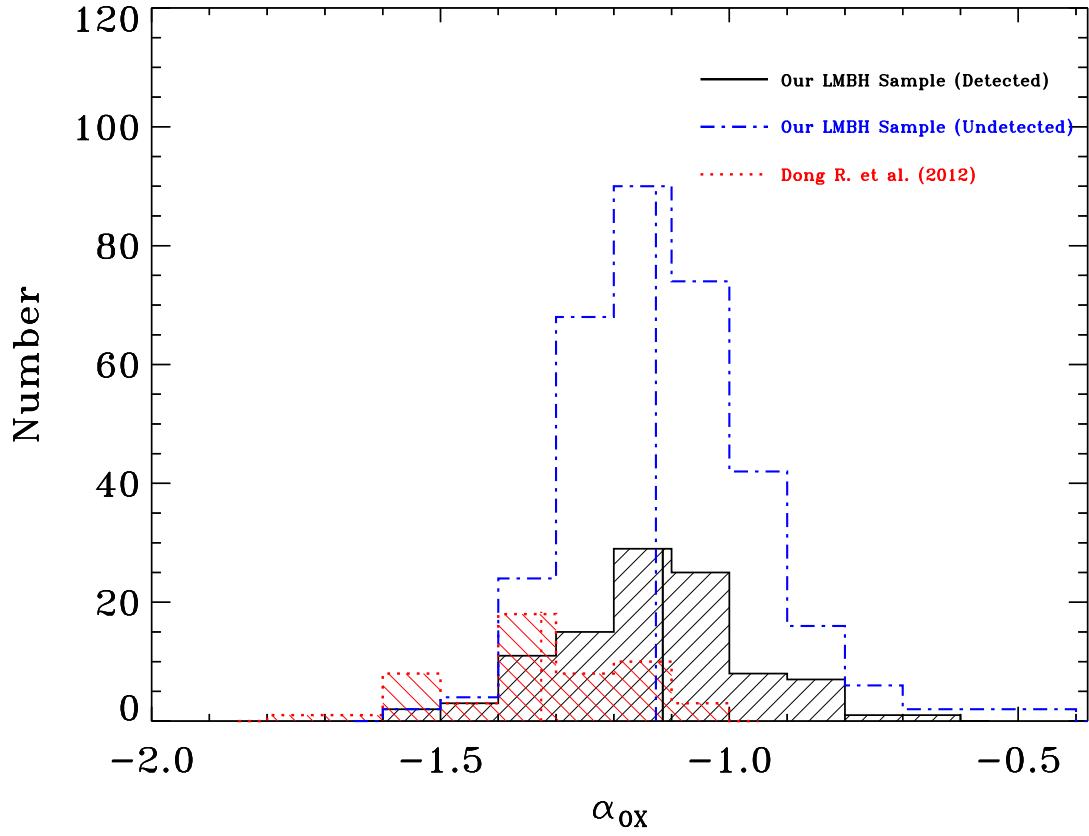


Fig. 7.— Distributions of  $\alpha_{OX}$  for objects detected with *ROSAT* in the total LMBH sample (black shaded histogram). *Chandra*-detected sources in Dong R. et al. (2012, red dotted shaded histogram) and upper limits for those undetected in *ROSAT* (blue dotted dashed histogram) in our sample are also plotted for comparison. The vertical lines represent the corresponding medians.

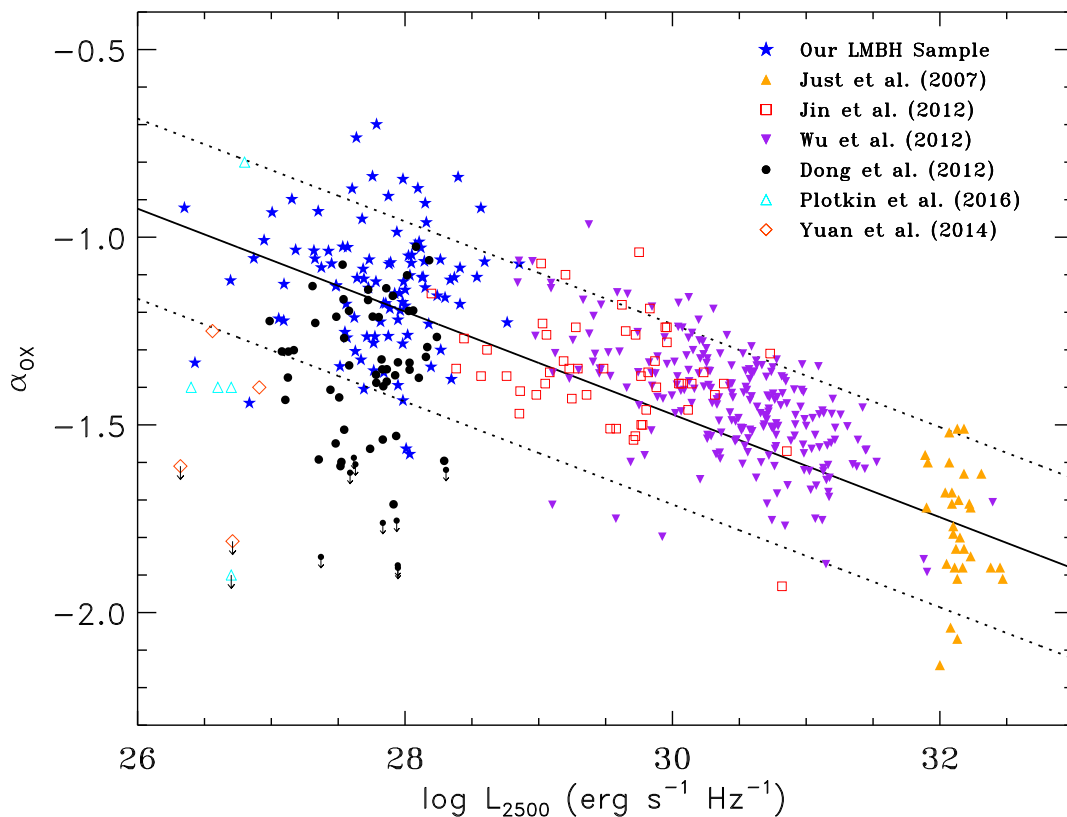


Fig. 8.— Optical-to-X-ray spectral index  $\alpha_{\text{OX}}$  versus the monochromatic luminosity at  $2500 \text{ \AA}$  for the total LMBH sample detected with *ROSAT* (blue filled star symbols). The  $2500 \text{ \AA}$  monochromatic luminosities are derived from  $L_{\text{H}\alpha\text{B}}$  using the scaling relation between  $L_{\text{H}\alpha\text{B}}$  and  $\lambda L_{\lambda}(5100 \text{ \AA})$  assuming a spectral shape of 1.56 ( $f_{\lambda} \propto \lambda^{-1.56}$ ). LMBHs in [Dong R. et al. \(2012\)](#), (black filled circles), [Yuan et al. \(2014\)](#), (orange red open diamonds) and [Plotkin et al. \(2016\)](#), (cyan open triangles), as well as more luminous Seyfert galaxies and QSOs in [Jin et al. \(2012\)](#), (red open squares), [Wu et al. \(2012\)](#), (purple filled inverted triangles) and [Just et al. \(2007\)](#), (orange filled triangles) are also plotted for comparison. The solid and dashed lines represent the relation and  $1 \sigma$  scatter given by [Steffen et al. \(2006\)](#), respectively. Arrows represent upper limits.

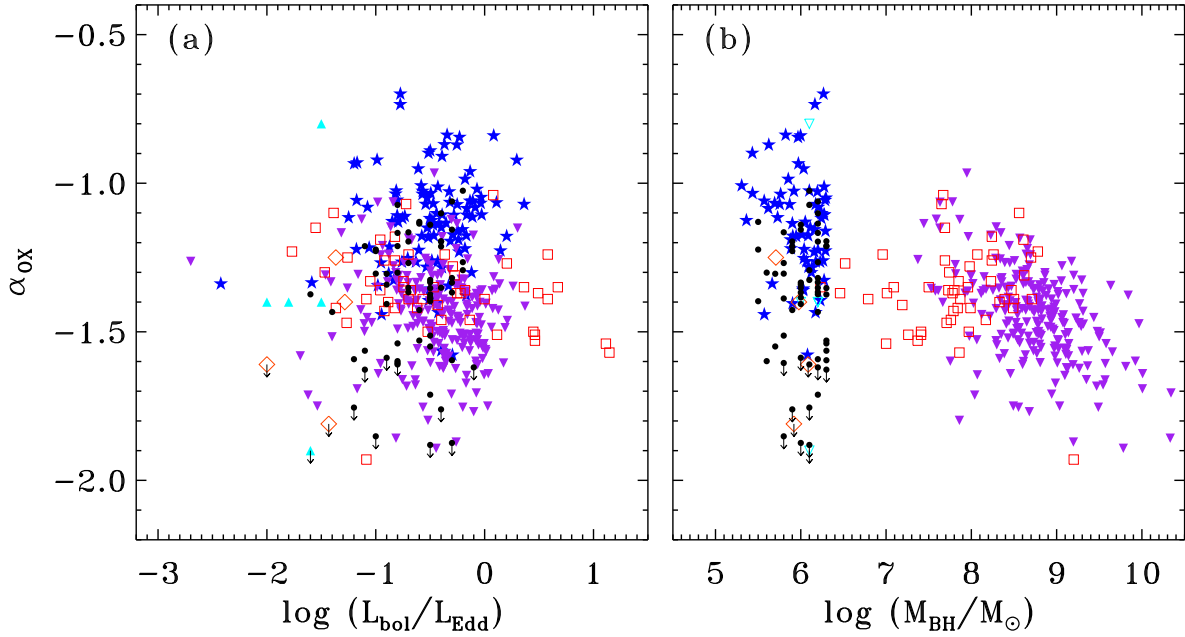


Fig. 9.— Dependence of the optical-to-X-ray spectral index  $\alpha_{OX}$  on Eddington ratio (a) and BH mass (b). The blue filled stars represent the total LMBH sample. Overplotted symbols are the low-mass AGNs with the Eddington ratios  $\log(L_{bol}/L_{Edd}) < -1$  from Yuan et al. (2014, orange red open diamonds) and Plotkin et al. (2016, cyan open triangles), LMBHs observed by *Chandra* from Dong R. et al. (2012, black filled circles), and more massive AGNs from Wu et al. (2012, purple filled inverted triangles) and Jin et al. (2012, red open squares), respectively. Arrows denote upper limits on  $\alpha_{OX}$ .

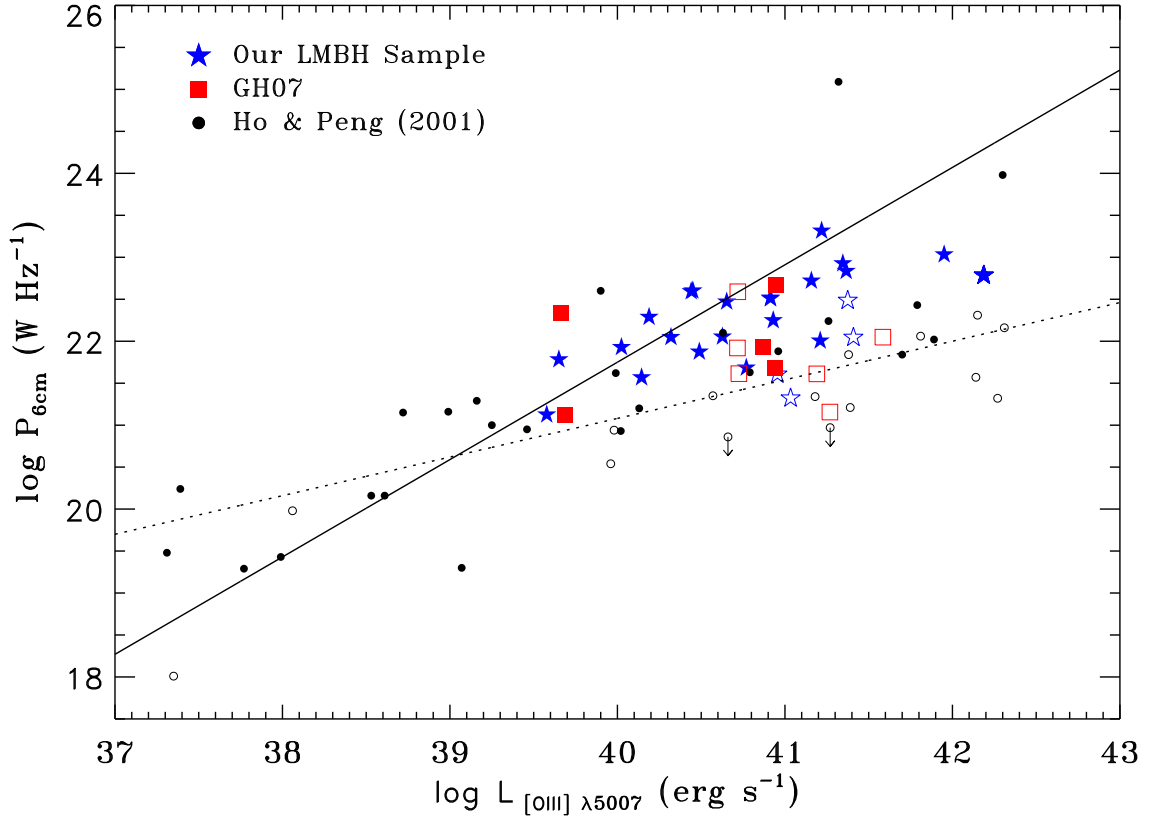


Fig. 10.— Relation of the radio power at 6 cm and the [O III]  $\lambda 5007$  luminosity for our total LMBH sample (blue stars), low-mass black holes from GH07 (red squares) and more massive Seyfert galaxies from Ho & Peng (2001, black circles). The filled and open symbols represent radio-loud and radio-quiet sources, respectively, and arrows denote upper limits. The solid and dashed lines represent the relation derived from more massive radio-loud and radio-quiet AGNs, respectively (Ho & Peng 2001).

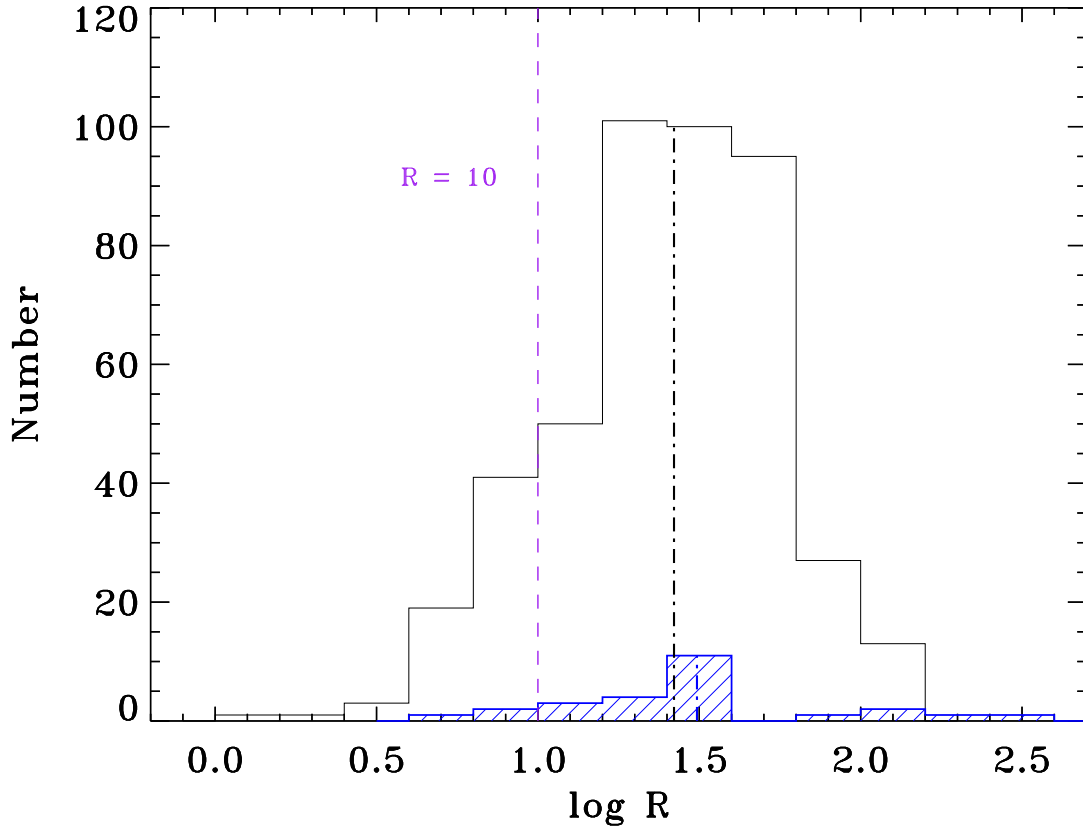


Fig. 11.— Distribution of the radio loudness of the total LMBH sample objects. Blue shaded histogram represents sources detected in the FIRST, while the black histogram represents upper limits derived assuming a flux density limit of 1 mJy at 20 cm for the FIRST survey. The conventional demarcation line between radio-loud and radio-quiet AGNs is marked by the dashed line. The dotted dashed lines denote corresponding medians.

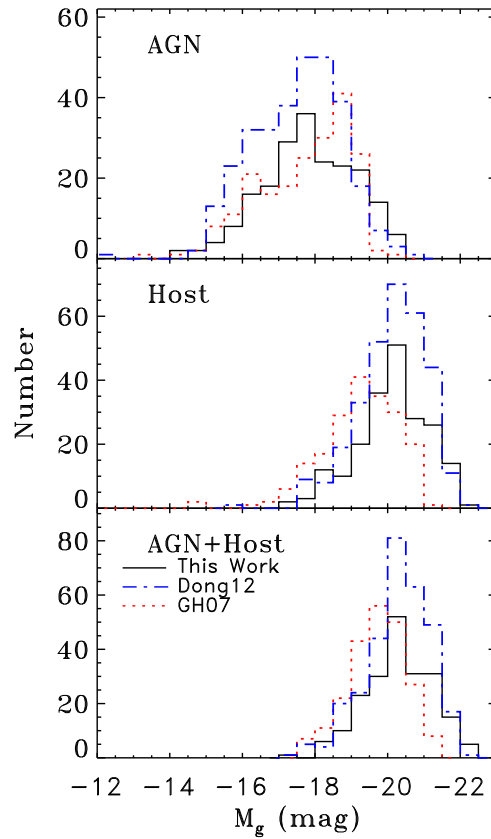


Fig. 12.— Distributions of the absolute  $g$ -band magnitudes of AGN (*top*), host galaxy (*middle*), and the total (AGN plus host galaxy) (*bottom*), for the sample in this work (black solid line), Dong+12 (blue dotted dashed line) and GH07 (red dotted line), respectively (see text for details of the estimation of the AGN and host galaxy luminosities.)

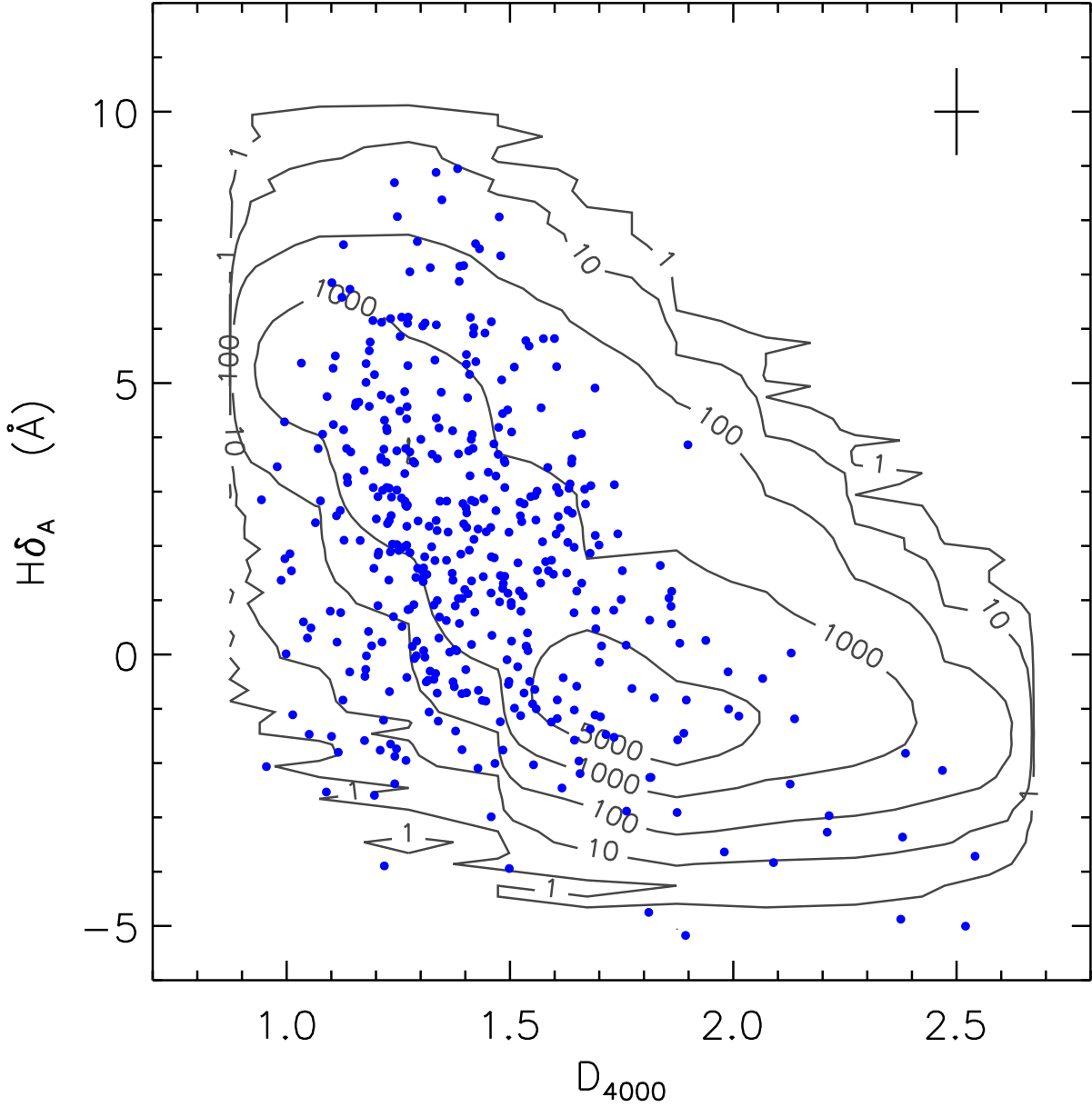


Fig. 13.— Distribution of 423 low-mass BH host galaxies (blue filled circles) from the total LMBH sample on the plane of 4000  $\text{\AA}$  break strength ( $D_{4000}$ ) versus equivalent width of the  $H\delta$  absorption ( $H\delta_A$ ). As a comparison, the distribution of  $\sim 492,000$  non-AGN galaxies in the SDSS DR7 is also plotted as contours. The cross at the upper-right corner represents the typical size of  $1\sigma$  errors.

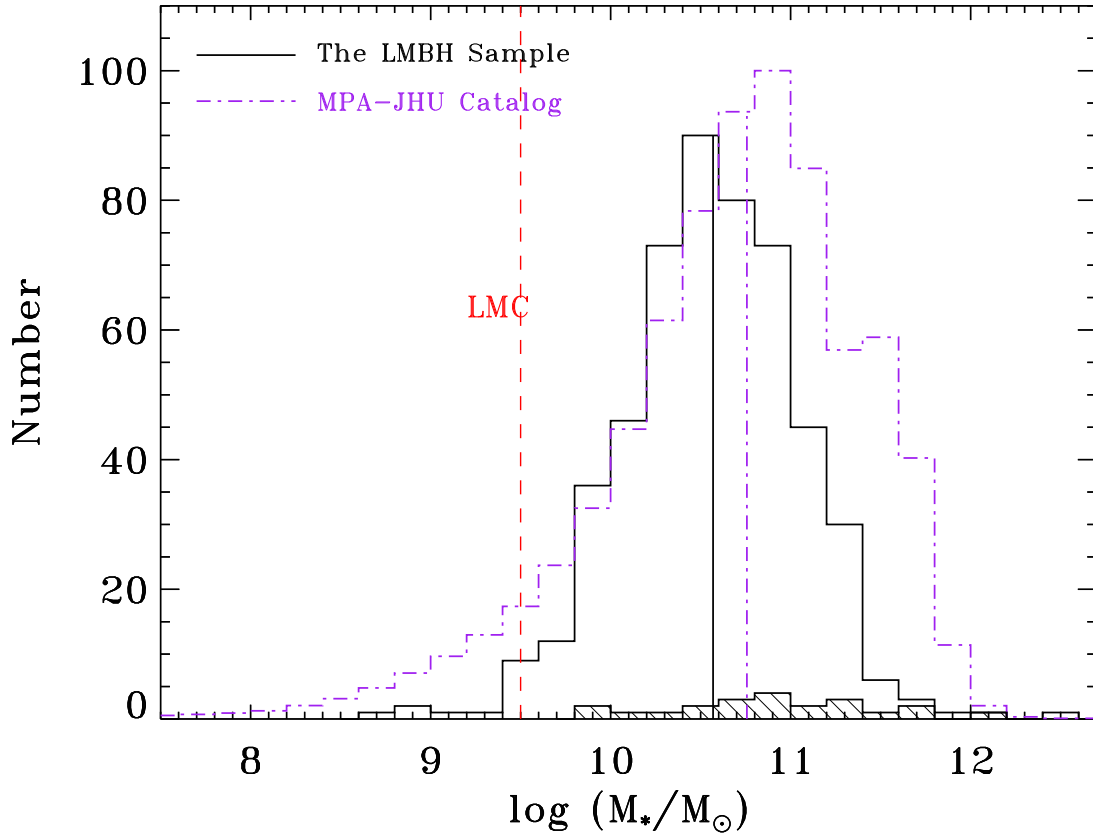


Fig. 14.— Distributions of the stellar masses ( $M_*$ ) of the host galaxies of our LMBH sample (black solid histogram) and  $\sim 925000$  sources in the SDSS DR7 of which the stellar masses are taken from the MPA–JHU catalog (purple dotted dashed histograms). The vertical lines represent the corresponding medians. The black shaded histogram represents radio-loud AGNs in our LMBH sample. (The MPA–JHU histogram is normalized to have a peak value of 100 for ease of comparison.)

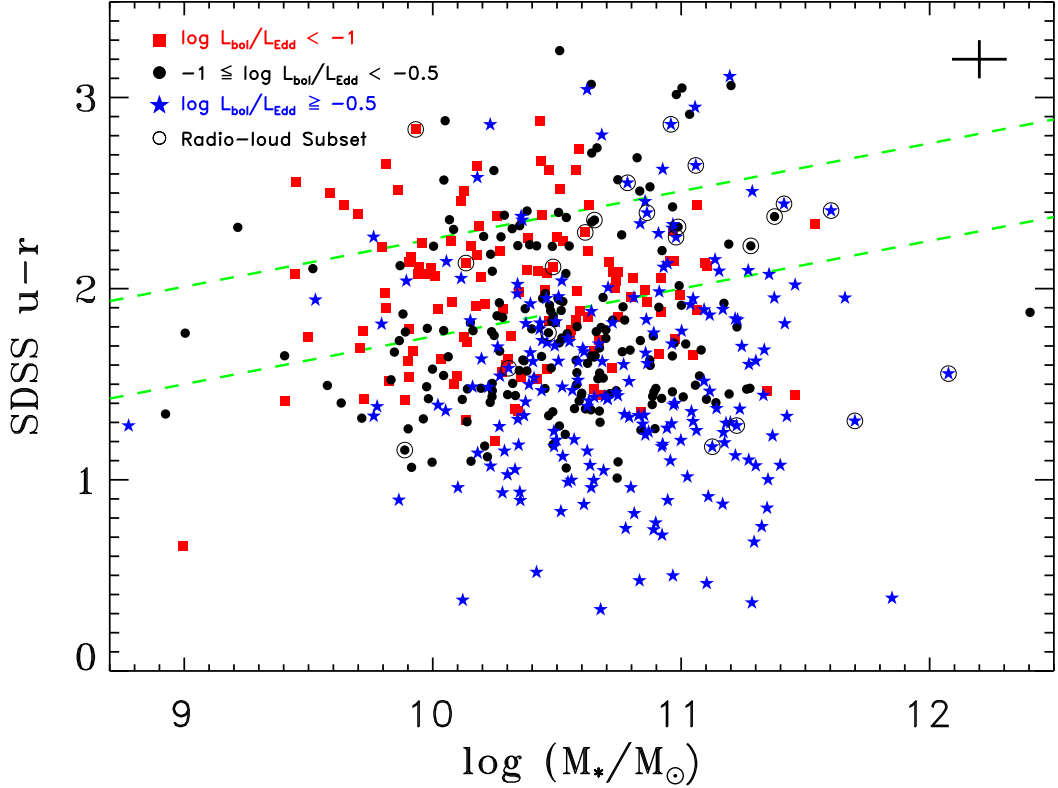


Fig. 15.— Distribution of the total LMBH sample on the the  $u-r$  color versus stellar mass plane. The green dashed lines denote the green valley defined by [Schawinski et al. \(2014\)](#). Red square, black filled circle and blue star represent sources with their Eddington ratios in the ranges of  $\log L_{\text{bol}}/L_{\text{Edd}} < -1$ ,  $-1 \leq \log L_{\text{bol}}/L_{\text{Edd}} < -0.5$  and  $\log L_{\text{bol}}/L_{\text{Edd}} \geq -0.5$ , respectively. Open circles denote radio-loud sources. Our LMBH sample objects span almost the entire  $u-r$  color range, and most of the objects are located in the green valley or blue sequence, while about 11% of the sample are in the red sequence. The cross at the upper right corner represents the typical size of  $1 \sigma$  errors.

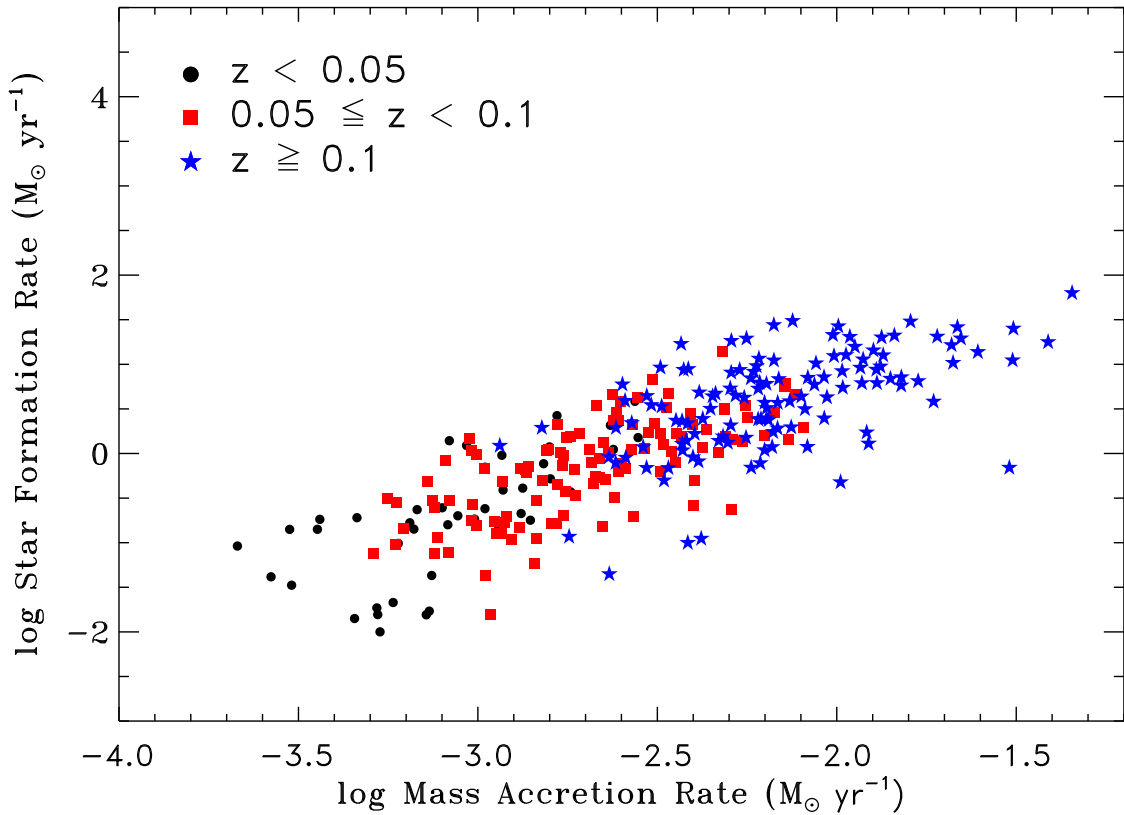


Fig. 16.— Mass accretion rate versus star formation rate for 282 sources in the total LMBH sample with AGN contribution lower than 75%. The mass accretion rates are derived assuming an efficiency of  $\eta=0.1$ . The star formation rates are obtained from the MPA–JHU catalog estimated using a technique described in [Brinchmann et al. \(2004\)](#). Blue stars, red squares and black circles represent sources with redshift  $z \geq 0.1$ ,  $0.05 \leq z < 0.1$  and  $z < 0.05$  respectively.

Table 1. The SDSS DR7 LMBH Sample

ID (1)	SDSS Name (2)	$z$ (3)	$g$ (4)	$g - r$ (5)	$A_g$ (6)
1	J054248.74+004019.2	0.0518	17.49	0.98	1.14
2	J074345.47+480813.5	0.0181	16.24	0.74	0.22
3	J080807.13+563832.4	0.0990	18.93	0.55	0.18

Note. — Col. (1): Identification number assigned in this paper. Col. (2): Official SDSS name in J2000.0. Col. (3): Redshift measured by the SDSS pipeline. Col. (4): Petrosian  $g$  magnitude, uncorrected for Galactic extinction. Col. (5): Petrosian  $g - r$  color. Col. (6): Galactic extinction in the  $g$  band. (*This table is available in its entirety in a machine-readable form in the online journal. A portion is shown here for guidance regarding its form and content.*)

Table 2: Emission-line Measurements

ID	[O II] $\lambda 3727$	Fe II $\lambda 4570$	H $\beta^N$	H $\beta^B$	[O III] $\lambda 5007$	[O I] $\lambda 6300$	H $\alpha^N$	H $\alpha^B$	[N II] $\lambda 6583$	[S II] $\lambda 6716$	[S II] $\lambda 6731$	FWHM <sub>H<math>\alpha^B</math></sub>	FWHM <sub>[O III]</sub>	FWHM <sub>[S II]</sub>
(1)	(2)	(3)	(4)	(5)	(6)	(7)	(8)	(9)	(10)	(11)	(12)	(13)	(14)	(15)
1	< -15.46	< -14.05	-15.57	< -15.54	-14.98	-15.73	-14.82	-14.70	-15.02	-15.59	-15.64	1986	227	133
2	...	< -14.54	-15.12	-14.92	-14.27	-15.16	-14.43	-13.95	-14.91	-15.00	-15.06	947	222	166
3	-14.80	-15.08	-14.99	-14.80	-14.38	-15.59	-14.39	-14.21	-14.62	-15.08	-15.20	1043	204	136

Note. — Col. (1): Identification number assigned in this paper. Cols. (2)–(12): Emission-line fluxes (or  $3\sigma$  upper limits) in log-scale, in units of  $\text{erg s}^{-1} \text{cm}^{-2}$ . The measured emission-line fluxes are regarded to be reliable detections if they have significance greater than  $3\sigma$ , or else the  $3\sigma$  values will be adopted as the upper limits. Note that these are observed values only corrected Galactic extinction, and no NLR or BLR extinction correction has been applied. The superscripts “N” and “B” in cols. 4, 5, 8, 9 and 13 refer to the narrow and broad components of the line, respectively. Cols. (13)–(15): Line widths (FWHM) that are calculated from the best-fit models and have been corrected for instrumental broadening using the values measured from arc spectra and tabulated by the SDSS; in units of  $\text{km s}^{-1}$ . (*This table is available in its entirety in a machine-readable form in the online journal. A portion is shown here for guidance regarding its form and content.*)

Table 3. Luminosity, Mass and Eddington Ratio Measurements

ID	$M_g(\text{total})$	$M_g(\text{AGN})$	$M_g(\text{host})$	$\log L_{\text{H}\alpha^{\text{B}}}$	$\log L_{[\text{O III}]\lambda 5007}$	$\log M_{\text{BH}}$	$\log L_{\text{bol}}/L_{\text{Edd}}$	$\log M_*$
(1)	(2)	(3)	(4)	(5)	(6)	(7)	(8)	(9)
1	−20.54	−15.78	−20.53	40.10	39.82	6.24	−1.61	10.65 <sup>a</sup>
2	−18.49	−15.38	−18.43	39.92	39.60	5.48	−1.01	9.80 <sup>a</sup>
3	−19.68	−18.12	−19.38	41.18	41.02	6.14	−0.58	10.04 <sup>c</sup>

Note. — Col. (1): Identification number assigned in this paper. Col. (2): Total  $g$ -band absolute magnitude. Col. (3): AGN  $g$ -band absolute magnitude, estimated from  $L_{\text{H}\alpha^{\text{B}}}$  given in col. (5) and a conversion from  $L_{\text{H}\alpha}$  to  $M_g$  assuming  $f_\lambda \propto \lambda^{-1.56}$ . Col. (4): Host galaxy  $g$ -band absolute magnitude, obtained by subtracting the AGN luminosity from the total luminosity. Col. (5): Luminosity of broad  $\text{H}\alpha$ , in units of  $\text{erg s}^{-1}$ . Col. (6): Luminosity of  $[\text{O III}]\lambda 5007$ , in units of  $\text{erg s}^{-1}$ . Col. (7): Virial mass estimate of the BH calculating following GH07 and Dong+12, in units of  $M_\odot$ . Col. (8): Eddington ratio. Col. (9): Stellar mass of the host galaxy. (*This table is available in its entirety in a machine-readable form in the online journal. A portion is shown here for guidance regarding its form and content.*)

<sup>a</sup>Estimated using the color– $M_*/L$  relation in [Into & Portinari \(2013\)](#) where color is the SDSS  $r - i$ , and  $L$  is the luminosity of 2MASS Ks-band.

<sup>b</sup>Estimated using the method similar with  $a$  but using UKIDSS K-band magnitude.

<sup>c</sup>Derived from MPA–JHU catalog.

<sup>d</sup>Estimated using the scaling relation between WISE  $3.4\mu\text{m}$  luminosity and stellar mass provided by [Wen et al. \(2013\)](#), which is calibrated by the stellar masses from the MPA–JHU catalog.

Table 4. *ROSAT* Detections

ID	Count Rate	$N_{\text{H}}$	$\Gamma$	$f_{0.5-2.0 \text{ keV}}$	$\log L_{0.5-2.0 \text{ keV}}$	$L_{2500}$	$\alpha_{\text{OX}}$
(1)	(2)	(3)	(4)	(5)	(6)	(7)	(8)
<i>Our new sample</i>							
6	$0.074 \pm 0.014$	4.40	$2.71^{+0.22}_{-0.23}$	$-12.24 \pm 0.08$	$42.31 \pm 0.08$	27.57	-1.27
27	$0.058 \pm 0.014$	3.10	$2.14^{+0.28}_{-0.31}$	$-12.35 \pm 0.11$	$43.94 \pm 0.11$	28.57	-0.92
34	$0.043 \pm 0.014$	3.50	...	$-12.49 \pm 0.14$	$42.76 \pm 0.14$	27.96	-1.19
37	$0.116 \pm 0.019$	3.60	$2.49^{+0.20}_{-0.22}$	$-12.08 \pm 0.07$	$42.88 \pm 0.07$	27.92	-1.15
39	$0.174 \pm 0.022$	1.70	$2.89^{+1.42}_{-1.33}$	$-12.32 \pm 0.06$	$42.34 \pm 0.06$	27.63	-1.30
45	$0.031 \pm 0.012$	1.50	$1.56^{+0.49}_{-0.67}$	$-12.63 \pm 0.16$	$43.29 \pm 0.16$	28.16	-0.96
47	$0.061 \pm 0.013$	2.60	$2.25^{+0.33}_{-0.34}$	$-12.40 \pm 0.10$	$42.63 \pm 0.10$	27.64	-1.11
59	$0.049 \pm 0.014$	1.60	...	$-12.67 \pm 0.12$	$42.77 \pm 0.12$	27.78	-1.12
75	$0.005 \pm 0.001$	2.10	$2.31^{+0.29}_{-0.33}$	$-13.59 \pm 0.05$	$40.86 \pm 0.05$	26.43	-1.33
82	$0.040 \pm 0.012$	1.80	...	$-12.72 \pm 0.12$	$42.92 \pm 0.12$	28.00	-1.14
87	$0.072 \pm 0.015$	1.70	...	$-12.49 \pm 0.09$	$43.68 \pm 0.09$	28.60	-1.06
96	$0.014 \pm 0.002$	1.40	$1.73 \pm 0.16$	$-13.05 \pm 0.05$	$41.84 \pm 0.05$	26.87	-1.06
99	$0.058 \pm 0.000$	1.60	...	$-12.60 \pm 0.00$	$43.29 \pm 0.00$	28.08	-1.02
100	$0.176 \pm 0.023$	2.30	$1.71^{+0.15}_{-0.17}$	$-11.84 \pm 0.06$	$43.27 \pm 0.06$	27.88	-0.89
103	$0.072 \pm 0.014$	1.40	$2.94^{+0.23}_{-0.28}$	$-12.79 \pm 0.09$	$43.31 \pm 0.09$	28.13	-1.11
104	$0.051 \pm 0.013$	1.20	...	$-12.73 \pm 0.11$	$43.45 \pm 0.11$	28.41	-1.08
110	$0.007 \pm 0.002$	2.60	$2.39 \pm 0.35$	$-13.39 \pm 0.10$	$42.63 \pm 0.10$	28.35	-1.38
117	$0.060 \pm 0.013$	1.30	$2.04 \pm 0.16$	$-12.52 \pm 0.09$	$41.71 \pm 0.09$	27.06	-1.22
118	$0.022 \pm 0.009$	1.10	...	$-13.12 \pm 0.18$	$42.66 \pm 0.18$	27.84	-1.18
121	$0.027 \pm 0.011$	1.10	...	$-13.04 \pm 0.17$	$41.93 \pm 0.17$	27.51	-1.34
123	$0.698 \pm 0.038$	1.20	$2.83^{+0.79}_{-0.76}$	$-11.81 \pm 0.02$	$43.55 \pm 0.02$	28.37	-1.11
124	$0.098 \pm 0.016$	1.10	$1.57^{+0.20}_{-0.22}$	$-12.19 \pm 0.07$	$43.48 \pm 0.07$	28.10	-0.87
125	$0.052 \pm 0.012$	1.10	...	$-12.74 \pm 0.10$	$42.59 \pm 0.10$	28.19	-1.35
126	$0.062 \pm 0.013$	1.20	$1.26^{+0.20}_{-0.21}$	$-12.30 \pm 0.09$	$42.79 \pm 0.09$	28.15	-1.13
130	$0.297 \pm 0.023$	1.20	$2.43^{+1.02}_{-1.01}$	$-12.00 \pm 0.03$	$42.74 \pm 0.03$	27.69	-1.11
132	$0.053 \pm 0.012$	0.90	...	$-12.79 \pm 0.10$	$43.36 \pm 0.10$	28.26	-1.06
135	$0.052 \pm 0.000$	1.10	$2.88^{+0.77}_{-0.75}$	$-12.99 \pm 0.00$	$42.03 \pm 0.00$	28.01	-1.56
138	$0.083 \pm 0.023$	2.00	...	$-12.38 \pm 0.12$	$42.83 \pm 0.12$	28.00	-1.18
144	$0.029 \pm 0.010$	1.40	$1.93^{+0.26}_{-0.27}$	$-12.78 \pm 0.15$	$43.06 \pm 0.15$	28.05	-1.05
150	$0.028 \pm 0.004$	1.60	$1.78 \pm 0.18$	$-12.73 \pm 0.06$	$42.97 \pm 0.06$	28.05	-1.07
155	$0.098 \pm 0.015$	1.00	...	$-12.49 \pm 0.07$	$43.25 \pm 0.07$	28.14	-1.06
165	$0.036 \pm 0.014$	1.90	...	$-12.75 \pm 0.17$	$43.30 \pm 0.17$	28.34	-1.11
166	$0.095 \pm 0.005$	2.40	$2.05 \pm 0.11$	$-12.18 \pm 0.02$	$42.74 \pm 0.02$	27.35	-0.93
176	$0.023 \pm 0.010$	3.80	...	$-12.73 \pm 0.18$	$42.45 \pm 0.18$	27.49	-1.13
177	$0.116 \pm 0.022$	3.90	$2.37^{+0.29}_{-0.33}$	$-12.03 \pm 0.08$	$42.55 \pm 0.08$	27.32	-1.04
186	$0.047 \pm 0.012$	5.50	...	$-12.32 \pm 0.11$	$42.38 \pm 0.11$	27.62	-1.21
190	$0.015 \pm 0.001$	3.50	$1.27^{+0.18}_{-0.23}$	$-12.78 \pm 0.04$	$41.56 \pm 0.04$	26.35	-0.92
192	$0.111 \pm 0.015$	1.70	$1.65^{+0.17}_{-0.18}$	$-12.09 \pm 0.06$	$43.46 \pm 0.06$	28.15	-0.91
<i>Dong+12</i>							
10	$0.050 \pm 0.013$	3.9	$2.53^{+0.27}_{-0.29}$	$-12.42 \pm 0.11$	$42.76 \pm 0.11$	27.86	-1.18
15	$0.030 \pm 0.014$	5.3	$2.56^{+0.37}_{-0.44}$	$-12.55 \pm 0.20$	$43.31 \pm 0.20$	27.94	-0.99
18	$0.024 \pm 0.004$	3.6	$1.55^{+0.16}_{-0.19}$	$-12.61 \pm 0.13$	$42.48 \pm 0.13$	27.15	-0.90
21	$0.067 \pm 0.019$	7.2	$2.42^{+0.17}_{-0.16}$	$-12.11 \pm 0.19$	$42.57 \pm 0.19$	27.82	-1.23
24	$0.026 \pm 0.011$	8.1	...	$-12.49 \pm 0.16$	$43.16 \pm 0.16$	28.30	-1.16

Table 4—Continued

ID (1)	Count Rate (2)	$N_{\text{H}}$ (3)	$\Gamma$ (4)	$f_{0.5-2.0 \text{ keV}}$ (5)	$\log L_{0.5-2.0 \text{ keV}}$ (6)	$L_{2500}$ (7)	$\alpha_{\text{OX}}$ (8)
27	0.026 ± 0.010	6.2	...	-12.54±0.08	42.21±0.08	27.55	-1.25
67	0.145 ± 0.025	2.8	2.91 <sup>+0.31</sup> <sub>-0.32</sub>	-12.20±0.13	42.83±0.13	27.43	-1.04
68	0.046 ± 0.014	3.0	2.39 <sup>+0.17</sup> <sub>-0.29</sub>	-12.52±0.11	43.19±0.11	28.03	-1.05
74	0.061 ± 0.015	4.9	3.83 <sup>+0.27</sup> <sub>-0.28</sub>	-12.55±0.08	42.75±0.08	27.84	-1.36
78	0.105 ± 0.019	4.3	3.06 <sup>+0.63</sup> <sub>-0.45</sub>	-12.18±0.12	43.60±0.12	28.11	-1.01
79	0.053 ± 0.014	3.7	3.96 <sup>+0.34</sup> <sub>-0.27</sub>	-12.86±0.08	43.98±0.08	28.76	-1.23
87	0.113 ± 0.022	1.7	3.24 <sup>+1.27</sup> <sub>-0.87</sub>	-12.66±0.16	42.26±0.16	27.69	-1.40
98	0.034 ± 0.013	1.6	...	-12.83±0.07	42.23±0.07	27.95	-1.39
99	0.107 ± 0.016	0.9	...	-12.48±0.13	44.03±0.13	28.40	-0.84
101	0.072 ± 0.000	0.7	...	-12.60±0.20	42.17±0.20	26.95	-1.01
102	0.040 ± 0.012	1.3	...	-12.82±0.14	42.68±0.14	27.89	-1.19
103	0.017 ± 0.008	2.5	...	-13.01±0.14	43.09±0.14	28.24	-1.16
105	0.033 ± 0.011	3.5	...	-12.60±0.06	42.76±0.06	27.53	-1.03
110	0.019 ± 0.002	3.0	2.61 <sup>+0.31</sup> <sub>-0.30</sub>	-12.95±0.12	42.47±0.12	27.18	-1.03
112	0.029 ± 0.009	1.3	...	-12.96±0.10	39.90±0.10	25.45	-1.34
115	0.127 ± 0.017	0.7	2.53 <sup>+0.15</sup> <sub>-0.14</sub>	-12.55±0.05	42.54±0.05	27.01	-0.93
117	0.002 ± 0.001	4.3	2.28 ± 0.05	-13.75±0.06	41.79±0.06	28.04	-1.58
123	0.046 ± 0.013	3.0	2.57 <sup>+0.27</sup> <sub>-0.22</sub>	-12.56±0.15	43.96±0.15	28.85	-1.07
125	0.067 ± 0.016	1.4	2.37 <sup>+0.42</sup> <sub>-0.36</sub>	-12.57±0.12	43.23±0.12	28.41	-1.18
135	0.005 ± 0.002	0.8	1.51 <sup>+0.05</sup> <sub>-0.06</sub>	-13.50±0.08	41.57±0.08	27.09	-1.22
138	0.099 ± 0.000	1.9	1.46 <sup>+0.33</sup> <sub>-0.28</sub>	-12.52±0.15	43.62±0.15	27.76	-0.84
149	0.032 ± 0.003	1.1	1.21 ± 0.13	-13.12±0.12	42.43±0.12	27.71	-1.26
153	0.115 ± 0.000	2.4	1.96 <sup>+0.30</sup> <sub>-0.41</sub>	-12.19±0.09	43.03±0.09	27.89	-1.07
163	0.176 ± 0.021	1.1	2.52 <sup>+0.52</sup> <sub>-0.44</sub>	-12.29±0.17	42.51±0.17	27.48	-1.13
164	0.226 ± 0.029	2.0	2.10 <sup>+0.11</sup> <sub>-0.12</sub>	-11.86±0.03	42.27±0.03	27.77	-1.28
169	0.041 ± 0.014	1.9	...	-12.70±0.13	42.40±0.13	27.56	-1.18
174	0.044 ± 0.012	1.2	...	-12.72±0.06	40.95±0.06	26.84	-1.44
175	0.101 ± 0.019	1.6	1.56 ± 0.16	-12.12±0.05	43.01±0.05	27.60	-0.87
183	0.030 ± 0.011	1.0	...	-13.01±0.09	42.46±0.09	27.37	-1.08
184	0.045 ± 0.012	1.4	...	-12.75±0.13	43.50±0.13	28.54	-1.11
196	0.101 ± 0.022	2.0	1.44 <sup>+0.30</sup> <sub>-0.32</sub>	-12.06±0.14	42.23±0.14	27.33	-1.06
203	0.021 ± 0.008	1.2	2.06 <sup>+0.77</sup> <sub>-0.96</sub>	-13.01±0.09	42.03±0.09	27.67	-1.33
212	0.396 ± 0.027	0.9	...	-11.91±0.07	43.67±0.07	27.98	-0.85
214	0.032 ± 0.010	1.7	...	-12.81±0.13	42.52±0.13	27.98	-1.28
217	0.125 ± 0.016	1.8	2.36 <sup>+0.31</sup> <sub>-0.33</sub>	-12.23±0.16	42.77±0.16	27.69	-1.08
221	0.121 ± 0.015	2.0	2.24 <sup>+0.17</sup> <sub>-0.16</sub>	-12.17±0.06	43.30±0.06	28.12	-1.03
229	0.041 ± 0.008	1.6	...	-12.75±0.07	42.97±0.07	27.88	-1.07
230	0.027 ± 0.008	1.8	...	-12.89±0.05	42.81±0.05	27.98	-1.17
232	0.043 ± 0.014	2.8	2.28 <sup>+0.37</sup> <sub>-0.28</sub>	-12.54±0.08	42.95±0.08	27.99	-1.12
235	0.055 ± 0.011	1.4	...	-11.90±0.09	43.62±0.09	27.64	-0.73
237	0.098 ± 0.016	1.5	2.89 <sup>+0.29</sup> <sub>-0.24</sub>	-12.61±0.07	43.04±0.07	28.18	-1.23
239	0.047 ± 0.014	2.6	2.17 <sup>+0.37</sup> <sub>-0.41</sub>	-12.55±0.12	41.72±0.12	26.70	-1.12
244	0.052 ± 0.005	1.3	1.69 <sup>+0.05</sup> <sub>-0.06</sub>	-12.58±0.02	42.76±0.02	27.96	-1.15
246	0.024 ± 0.009	1.0	1.63 ± 0.15	-12.83±0.06	42.35±0.06	27.45	-1.07
249	0.095 ± 0.013	1.4	2.20 <sup>+0.52</sup> <sub>-0.46</sub>	-12.36±0.08	43.10±0.08	28.14	-1.11

Table 4—Continued

ID (1)	Count Rate (2)	$N_{\text{H}}$ (3)	$\Gamma$ (4)	$f_{0.5-2.0 \text{ keV}}$ (5)	$\log L_{0.5-2.0 \text{ keV}}$ (6)	$L_{2500}$ (7)	$\alpha_{\text{OX}}$ (8)
252	$0.073 \pm 0.012$	1.4	$2.49^{+0.16}_{-0.18}$	$-12.59 \pm 0.12$	$42.72 \pm 0.12$	27.95	-1.22
253	$0.107 \pm 0.013$	1.7	$1.96^{+0.37}_{-0.42}$	$-12.18 \pm 0.10$	$42.95 \pm 0.10$	28.04	-1.10
256	$0.103 \pm 0.018$	1.5	$2.87^{+0.39}_{-0.38}$	$-12.58 \pm 0.14$	$42.67 \pm 0.14$	27.88	-1.26
259	$0.038 \pm 0.008$	1.3	$2.61^{+0.46}_{-0.45}$	$-12.95 \pm 0.18$	$42.93 \pm 0.18$	27.73	-1.06
263	$0.185 \pm 0.028$	2.4	$3.37^{+0.40}_{-0.45}$	$-12.34 \pm 0.14$	$42.76 \pm 0.14$	27.77	-1.26
269	$0.042 \pm 0.011$	6.6	$3.36 \pm 0.10$	$-12.44 \pm 0.06$	$42.99 \pm 0.06$	28.02	-1.26
271	$0.895 \pm 0.035$	1.3	$2.55 \pm 1.21$	$-11.55 \pm 0.00$	$42.89 \pm 0.00$	27.57	-1.03
276	$0.088 \pm 0.013$	1.3	...	$-12.40 \pm 0.04$	$42.03 \pm 0.04$	27.10	-1.12
284	$0.017 \pm 0.003$	2.5	$2.65^{+0.78}_{-1.06}$	$-13.09 \pm 0.15$	$42.24 \pm 0.15$	27.77	-1.36
286	$0.017 \pm 0.005$	2.8	$1.51^{+0.52}_{-0.61}$	$-12.81 \pm 0.19$	$42.84 \pm 0.19$	27.68	-0.95
287	$0.022 \pm 0.005$	3.1	$2.20^{+0.53}_{-0.52}$	$-12.79 \pm 0.00$	$42.62 \pm 0.00$	27.73	-1.14
289	$0.034 \pm 0.011$	5.0	$3.34^{+1.23}_{-1.18}$	$-12.66 \pm 0.03$	$42.51 \pm 0.03$	27.98	-1.43
297	$0.021 \pm 0.009$	4.9	$3.20^{+0.75}_{-0.73}$	$-12.85 \pm 0.00$	$43.05 \pm 0.00$	28.27	-1.30
301	$0.045 \pm 0.014$	2.9	$2.20^{+0.89}_{-0.88}$	$-12.49 \pm 0.04$	$43.76 \pm 0.04$	27.79	-0.70

Note. — Col. (1): Identification number assigned in this paper and Dong+12 respectively. Col. (2): *ROSAT* count rate (count s<sup>-1</sup>). Col. (3): Galactic column density  $N_{\text{H}}$  (10<sup>20</sup> cm<sup>-2</sup>). Col. (4): Photon index of X-ray spectrum. Col. (5): X-ray flux in the 0.5–2.0 keV in log-scale (erg s<sup>-1</sup> cm<sup>-2</sup>). Col. (6): X-ray luminosity in the 0.5–2.0 keV in log-scale (erg s<sup>-1</sup>). Col. (7): Monochromatic luminosity at 2500 Å (erg s<sup>-1</sup> Hz<sup>-1</sup>). Col. (8): Optical-to-X-ray effective spectral index  $\alpha_{\text{OX}}$ .

Table 5. FIRST Detections

ID	$S_{20\text{cm}}$	$\log P_{20\text{cm}}$	$\log R$
(1)	(2)	(3)	(4)
<i>Our new sample</i>			
23	$1.14 \pm 0.16$	$22.80 \pm 0.06$	1.36
28	$0.85 \pm 0.15$	$22.15 \pm 0.07$	1.22
55	$2.86 \pm 0.19$	$22.32 \pm 0.03$	1.49
89	$1.22 \pm 0.16$	$22.89 \pm 0.06$	1.51
95	$16.75 \pm 0.86$	$23.59 \pm 0.02$	2.49
123	$2.72 \pm 0.19$	$22.76 \pm 0.03$	1.05
143	$1.97 \pm 0.17$	$22.20 \pm 0.04$	1.51
199	$2.67 \pm 0.18$	$22.27 \pm 0.03$	0.80
201	$1.79 \pm 0.16$	$23.07 \pm 0.04$	1.34
<i>Dong+12</i>			
22	$1.82 \pm 0.14$	$22.32 \pm 0.03$	1.57
30	$3.18 \pm 0.27$	$23.12 \pm 0.04$	2.03
36	$4.53 \pm 0.26$	$23.32 \pm 0.03$	2.06
54	$2.07 \pm 0.18$	$22.75 \pm 0.04$	1.43
78	$1.44 \pm 0.17$	$22.88 \pm 0.05$	1.44
118	$1.04 \pm 0.14$	$21.87 \pm 0.06$	0.84
140	$2.38 \pm 0.19$	$22.05 \pm 0.03$	1.57
141	$2.55 \pm 0.18$	$21.83 \pm 0.03$	1.58
170	$1.03 \pm 0.16$	$21.95 \pm 0.07$	1.58
181	$1.29 \pm 0.16$	$22.32 \pm 0.06$	0.91
206	$2.33 \pm 0.18$	$21.39 \pm 0.03$	1.49
208	$8.81 \pm 0.46$	$23.20 \pm 0.02$	2.21
222	$2.69 \pm 0.20$	$21.58 \pm 0.03$	1.15
257	$2.52 \pm 0.19$	$22.56 \pm 0.03$	1.50
273	$1.43 \pm 0.16$	$22.53 \pm 0.05$	1.09
277	$0.68 \pm 0.14$	$23.02 \pm 0.09$	1.36
305	$3.78 \pm 0.23$	$22.79 \pm 0.03$	1.98

Note. — Col. (1): Identification number assigned in this paper and Dong+12 respectively. Col. (2): Flux density at 20 cm from the FIRST (mJy). Uncertainties include the 5% systematic uncertainty recommended by White et al. (1997). Col. (3): Corresponding radio power ( $\text{W Hz}^{-1}$ ) at 20 cm. Col. (4): Radio loudness in log-scale.  $R \equiv f_{6\text{cm}}/f_{4400\text{\AA}}$  assuming a spectral index of  $\alpha_r = 0.46$  (radio; Ulvestad & Ho 2001) and  $\alpha_o = 0.44$  (optical; Vanden Berk et al. 2001), where  $f_\nu \propto \nu^{-\alpha_o}$ .